

TUNL REU IV

RESEARCH REPORT

20 MAY 2018 – 28 JULY 2018



TRIANGLE UNIVERSITIES NUCLEAR LABORATORY

Duke University  
North Carolina Central University  
North Carolina State University  
University of North Carolina at Chapel Hill

Box 90308, Durham, North Carolina 27708-0308, USA

The research described in this report is supported by the United States Department of Energy, Office of Science, under:

Grant No. DE-SC0010007 (Duke University High-Energy Physics Group),  
Grant No. DE-FG02-97ER41033 (Duke University/TUNL),  
Grant No. DE-FG02-97ER41042 (North Carolina State University), and  
Grant No. DE-FG02-97ER41041 (University of North Carolina).

The TUNL Research Experiences for Undergraduates (REU) Program is supported by the National Science Foundation under:

Grant No. NSF-PHY-1757783.

# Contents

<b>Introduction</b>	<b>iv</b>
<b>Personnel</b>	<b>v</b>
<b>1 Research Based at Duke</b>	<b>1</b>
1.1 Thickness and Composition Analysis of $^{24}\text{Mg}$ Targets from a Modified Evaporator . . . . .	2
1.2 Background Measurement of Gamma Rays, Muons, and Neutrons at LENA . . . . .	4
1.3 Studying the Response of a Cerium Bromide Scintillator for Nuclear Structure Studies at HI $\gamma$ S	6
1.4 Construction of a Wire Chamber for Reactor Neutrino Studies . . . . .	8
1.5 Characterizing NaI[Tl] Scintillating Crystals for the COHERENT Experiment . . . . .	10
1.6 Event Generator for Neutrinos on Deuterons . . . . .	12
1.7 Ionization Chamber Development for the Detection of Tritium . . . . .	14
1.8 Development of a Rutherford Backscattering Spectrometry Station for TUNL . . . . .	16
1.9 Application of Fourier Analysis to SQUID Systems in the NEDM EXPERIMENT . . . . .	18
<b>2 Research Based at CERN</b>	<b>20</b>
2.1 Tagging Quark and Gluon Jets Reconstructed by Particle Flow . . . . .	21
2.2 Identifying Quarks and Gluons Using Dijet Event Kinematics . . . . .	23
2.3 Boosted Decision Trees Enhanced for Supersymmetry Search . . . . .	25
2.4 Study of backgrounds for $X \rightarrow W\gamma$ search at $\sqrt{S} = 13$ TeV . . . . .	27

# Introduction

An important national goal is to develop a diverse, internationally competitive, and globally engaged workforce in science and engineering. The Research Experiences for Undergraduates (REU) program is part of the effort to achieve that goal. The REU program at the Triangle Universities Nuclear Laboratory (TUNL) and Duke University provides a ten-week opportunity for undergraduate students to pursue research in the areas of nuclear and particle physics. This allows promising physics majors to broaden their education through participation in research at the frontiers of these exciting scientific fields.

In 2018, thirteen students participated in the TUNL REU Program: nine spent the summer working on nuclear physics projects on the Duke campus, while the other four spent four weeks at Duke and six weeks at the European Center for Nuclear Research (CERN) near Geneva, Switzerland, working on particle physics projects. Having the nuclear and particle physics students in the same program facilitated cross-field intellectual exchange and the sharing of resources needed by both groups, while the participation of the Duke high energy physics group in the program gives it an international component.

Through introductory lectures and direct research involvement, the students gain experience and insights in the main stages of scientific research in nuclear and particle physics:

- The development of concepts to probe specific features of nuclear matter, particles and fields;
- The design, construction, testing, and installation of equipment and instrumentation;
- Data acquisition, analysis, and interpretation; and
- The dissemination of research results.

In addition to direct involvement in research projects, the REU program at Duke includes activities that are designed to broaden the students' physics foundation, enhance their research skills, and build confidence. These activities include: (1) regular meetings with the program coordinator, (2) research tutorials and special topic lectures, (3) a science writing tutorial, and (4) a required report and presentation by each student at the end of the program. The research reports written by the students form the main body of this document.

# Personnel

## 2018 TUNL REU Participants

<i>Student</i>	<i>Home Institution</i>	<i>Faculty Advisor</i>	<i>Class</i>
Phoebe Amory	Wellesley College	Ayana Arce	So
Muhammad Aziz	Adelphi University	Al Goshaw	Jr
Allyson Brodzeller	Bowling Green State University	Ayana Arce	Jr
Thomas Chappelow	North Carolina State University	Art Champagne	Jr
Jesse Devaney	Indiana University	Phil Barbeau	Jr
Pierce Giffin	University of Kansas	Robert Golub	So
Adrian Gutierrez	University of Oregon	Ayana Arce	Jr
Hannah Hasan	Ohio State University	Phil Barbeau	So
Samantha Johnson	Boise State University	Robert Janssens	Jr
Jessica Koros	Florida State University	Kate Scholberg	Jr
Katherine Parham	Hendrix College	Calvin Howell	Jr
Andrew Wantz	Indiana Wesleyan University	Richard Longland	So
Clay Wegner	Angelo State University	Art Champagne	Jr

## 2018 TUNL REU Administration

*Principal Investigator and Program Director:*

Dr. Alexander Crowell

*Co-Principal Investigator and CERN Experience Director:*

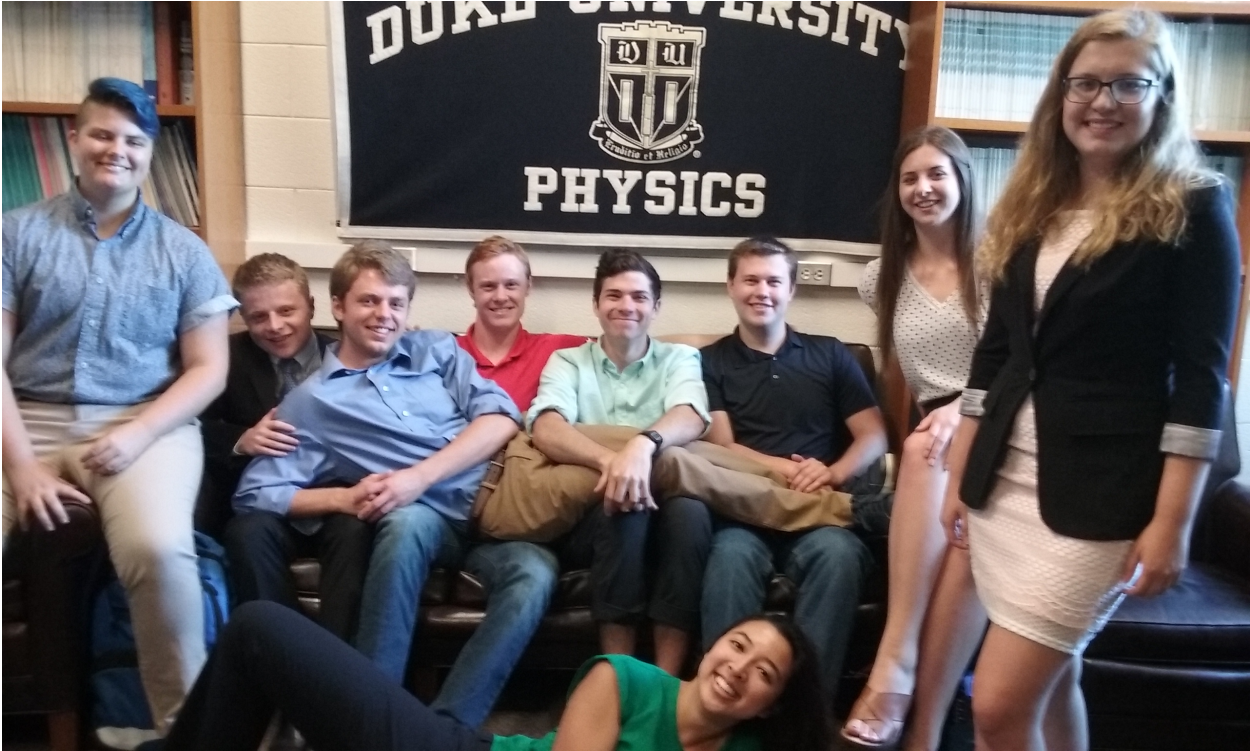
Professor Ayana Arce



PARTICIPANTS IN THE TUNL RESEARCH EXPERIENCES FOR UNDERGRADUATES (REU) PROGRAM ARE SHOWN ON THE DUKE CAMPUS. SHOWN IN THE PHOTOGRAPH FROM LEFT TO RIGHT ARE: (FRONT ROW) PIERCE GIFFIN (UNIVERSITY OF KANSAS), ALLYSON BRODZELER (BOWLING GREEN STATE UNIVERSITY), ANDREW WANTZ (INDIANA WESLEYAN UNIVERSITY) ADRIAN GUTIERREZ (UNIVERSITY OF OREGON); (MIDDLE ROW) KATHERINE PARHAM (HENDRIX COLLEGE), PHOEBE AMORY (WELLESLEY COLLEGE), HANNAH HASAN (OHIO STATE UNIVERSITY), JESSICA KOROS (FLORIDA STATE UNIVERSITY); (BACK ROW) SAMANTHA JOHNSON (BOISE STATE UNIVERSITY), CLAY WEGNER (ANGELO STATE UNIVERSITY), JESSE DEVANEY (INDIANA UNIVERSITY), THOMAS CHAPPELOW (NORTH CAROLINA STATE UNIVERSITY), MUHAMMAD AZIZ (ADELPHI UNIVERSITY).

# Research Based at Duke

Chapter 1



## 1.1 Thickness and Composition Analysis of $^{24}\text{Mg}$ Targets from a Modified Evaporator

T. CHAPPELOW, *North Carolina State University, Raleigh, NC*; D. LITTLE, A.E. CHAMPAGNE, *TUNL*

A project to measure the strength of the  $^{25}\text{Mg}(p,\gamma)^{26}\text{Al}$  proton capture reaction at 92.2 keV is planned. We modified a standard target evaporator with a custom water cooling system and assessed its ability to produce viable  $^{25}\text{Mg}$  targets for this future study. A line of Mg targets was produced with the new evaporator and the composition of one of the targets was assessed using beam from the LENA JN source. Results suggested that the new evaporator is able to produce extremely viable  $^{25}\text{Mg}$  targets.

There is considerable uncertainty in current measurements of the strength of the  $^{25}\text{Mg}(p,\gamma)^{26}\text{Al}$  proton capture reaction around the resonance energy of 92.2 keV. As this is the resonance that typically dominates at temperature ranges of  $T_9 \approx 0.6 - 1.4$ , accurate measurement of this strength will improve understanding of how much  $^{26}\text{Al}$  can be produced by massive stars [Str12, Ili11].

In response, a project is planned to directly measure the 92.2 keV resonance strength of the  $^{25}\text{Mg}(p,\gamma)^{26}\text{Al}$  reaction, using the Electron Cyclotron Resonance (ECR) source located in the Laboratory for Experimental Nuclear Astrophysics (LENA). Proton beams generated by this source will be accelerated to 92.2 keV in the center of mass frame to strike a  $^{25}\text{Mg}$  target made in-house. The reaction yield will be measured using a high resolution HPGe detector, along with a Ge - NaI coincidence setup [Cha16].

In order to produce viable  $^{25}\text{Mg}$  targets for this project, we modified a standard target evaporator with a new water-cooled target holder (see Fig. 1.1). Target cooling was expected to inhibit the re-evaporation of  $^{25}\text{Mg}$  deposited on the target backing which should produce especially thick and pure targets and thus reduce the time required for data on the reaction rates to be taken. The purpose of this study was to assess the ability of this modified evaporator to produce appropriate  $^{25}\text{Mg}$  targets for these future runs.

After installing the evaporator modifications, a line of tantalum-backed targets were made using the new setup.  $^{24}\text{Mg}$  was used to form the reactant layer for each target. As  $^{24}\text{Mg}$  is much cheaper than  $^{25}\text{Mg}$ , and chemically similar in terms of how it evaporates, the quality of these targets would be almost identical to the quality of their  $^{25}\text{Mg}$  counterparts.

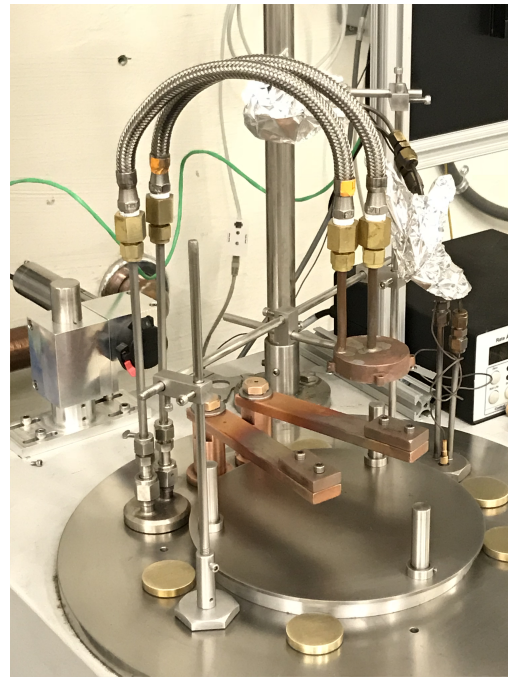


**Figure 1.1:** Newly modified evaporator stage. 55° water is pumped through suspended copper block, responsible for holding target backing above evaporated source.

The targets were prepared from standard tantalum backings, which were initially etched using a sulfuric acid bath. After outgassing, gold was evaporated onto each backing in order to prevent magnesium from migrating into the tantalum (with the cooling system turned off).  $^{24}\text{Mg}$  was then evaporated onto each backing with the new cooling system turned on, and the resulting targets were stored in low vacuum.

A total of four  $^{24}\text{Mg}$  targets were made. Among them, one target was chosen at random and placed inside the target area connected to the LENA JN, once the accelerator was fully prepared.

Over the course of four hours, proton beams generated from the JN were used to bombard the target. For each separate run, the beam energy ranged from 415 to 474 keV, with  $418.4 \pm 0.4$  keV being a relatively well-understood resonance energy for the  $^{24}\text{Mg}(p,\gamma)^{25}\text{Al}$  reaction. Reaction yields for each run were measured with a HPGe detector oriented at  $55^\circ$  relative to the beam line.

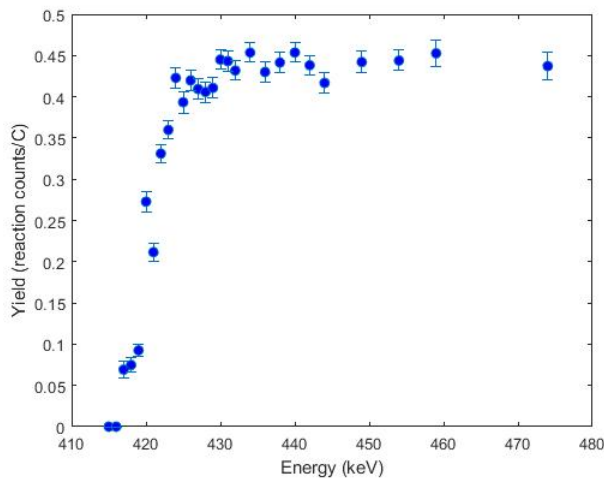


**Figure 1.2:**  $\text{Mg}^{24}(p,\gamma)\text{Al}^{25}$  reaction yield as a function of proton beam energy. The absence of a 'drop-off' in yield with increasing energy suggests that the target  $^{24}\text{Mg}$  layer is extremely thick.

The thickness of the  $^{24}\text{Mg}$  target in question was assessed qualitatively by analyzing the reaction yield curve. Current experimental models heavily correlate target thickness and slower declines in reaction yield as beam energies move away from resonance values.

The purity of the target layer, equivalently, the number of active  $^{24}\text{Mg}$  nuclei per square centimeter over the number of  $^{16}\text{O}$  nuclei per square centimeter,  $n_{\text{Mg}}/n_{\text{O}}$ , can be determined from the equation

$$\epsilon_{\text{eff}} = \epsilon_{\text{Mg}} + (n_{\text{O}}/n_{\text{Mg}})\epsilon_{\text{O}} \quad (1.1)$$

where  $\epsilon_{\text{eff}}$ ,  $\epsilon_{\text{O}}$ ,  $\epsilon_{\text{Mg}}$  are the effective stopping power of the target layer, the stopping power of pure oxygen, and the stopping power of pure  $^{24}\text{Mg}$ , respectively [Ili07].  $\epsilon_{\text{eff}}$  was calculated directly from

$$Y_{\text{max},\Delta E=\infty} = \omega\gamma(\lambda_{\text{eff}})^2/2\epsilon_{\text{eff}} \quad (1.2)$$

with  $\omega\gamma$ , in this case, being the strength of the  $^{24}\text{Mg}(p,\gamma)^{25}\text{Al}$  reaction at the beam energy at which the yield was maximized (in this case, 434 keV).  $Y_{\text{max},\Delta E=\infty}$  was the maximum reaction yield attained at 434 keV.  $\lambda_{\text{eff}}$  was the associated de Broglie wavelength at this energy [Ili07].

Overall, our results from these JN runs were extremely promising. The  $^{24}\text{Mg}(p,\gamma)^{25}\text{Al}$  yield experienced very little drop as beam energies strayed away from resonance (see Fig. 1.2). Our calculations from the maximum reaction yield yielded a purity value of 69.5%  $^{24}\text{Mg}$ .

The yield curve suggests that the  $^{24}\text{Mg}$  layer was extremely thick, resulting in a high incidence of reactions resulting from lower-energy protons penetrating the target. The purity value measured from our yields was nearly twice as large as values measured from conventionally-prepared  $^{24}\text{Mg}$  targets.

In terms of future work, repeated runs on other targets must be made in order to corroborate our results here. Once the viability of this target-making process is properly established, we can begin production of  $^{25}\text{Mg}$  targets to finally measure the strength of the  $^{25}\text{Mg}(p,\gamma)^{26}\text{Al}$  reaction at the 92.2 keV resonance.

[Cha16] A. E. Champagne and C. Iliadis, 2016, unpublished.

[Ili07] C. Iliadis, *Nuclear Physics of Stars*, Wiley-VCH, 2007.

[Ili11] C. Iliadis *et al.*, *Astrophys. J. Supp.*, **193**, 16 (2011).

[Str12] F. Streider *et al.*, *Phys. Lett.*, **B707**, 60 (2012).

## 1.2 Background Measurement of Gamma Rays, Muons, and Neutrons at LENA

C. WEGNER, *Angelo State University, San Angelo, TX*; A.E. CHAMPAGNE, *TUNL*

The Laboratory for Experimental Nuclear Astrophysics (LENA) will be replacing its existing 1-MeV JN accelerator with a 2-MeV singletron whose size would be better accommodated by switching the location of the target from the east end of the lab to the west end. However, the amount of background radiation may be different at opposite ends of the lab due to the construction of the building. The goal of this project was to measure the flux of  $\gamma$ -ray, muon, and neutron background radiation at the target's current eastern location and at the west end of the lab to determine the feasibility of relocating the target. Measurements indicate that the muon and neutron backgrounds at the current target location are lower than at the west end, but that the background from  $\gamma$  rays is higher.

Experiments in nuclear astrophysics are often characterized by low count rates from the reaction of interest and much higher count rates from sources of background radiation, which obscure information produced by the studied reaction [Lon06]. Any project therefore aims to reduce the amount of background by as much as possible through either active or passive measures. The simplest passive method of reducing unwanted background is to place the target location in a shielded area, or in the area with the lowest possible natural background.

At LENA, the size of the new accelerator would be better accommodated if the orientation of the lab was switched, moving the location of the target from the east end to the west. This project examines how the background levels of  $\gamma$  rays, muons, and neutrons differ between the east and west ends of LENA to determine if a switch is feasible.

Gamma rays are produced in the particle showers created when cosmic rays collide with atmospheric molecules, but are primarily generated environmentally via the decay chains of uranium, thorium, and potassium. Namely, the ubiquitous lines from  $^{208}\text{Tl}$  and  $^{40}\text{K}$  contribute heavily to any gamma ray spectrum.

The environmental  $\gamma$ -ray background at LENA was measured using HPGe and NaI detectors. Spectra from each detector were loaded into the JAM nuclear data acquisition software and calibrated according to the known 1461 keV and 2615 keV peaks of  $^{40}\text{K}$  and  $^{208}\text{Tl}$ , respectively. Then, the spectra were integrated up to a threshold of 3 MeV, since this is the upper limit at which most environmental

gamma rays are emitted. As seen in Fig. 1.3, both detectors counted more gamma rays at the east end.

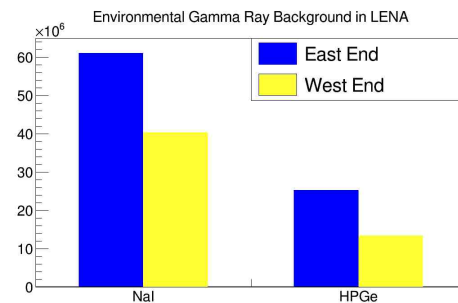


Figure 1.3:  $\gamma$ -ray counts at each location as recorded by NaI and HPGe detectors.

Due to a higher detection efficiency, the NaI spectrum also included information about cosmogenic  $\gamma$  rays, which are created at energies over 3 MeV. In the case of these  $\gamma$  rays, the background is lower at the east end than at the west end. However, there are fewer cosmic ray-induced  $\gamma$  rays than environmental by a margin of 2-3 orders of magnitude. Therefore, the  $\gamma$ -ray background at the east end is still considerably higher than at the west end of LENA.

Muons are also produced in cosmic ray-induced particle showers. They are highly penetrating and easily reach the surface, causing pair production, interacting with nuclei, and emitting bremsstrahlung as they slow, all of which contribute to the background [Heu95].

The muon background at both locations in LENA was measured with a BC-408 plastic scintillation de-

tector. At each location, the detector was run for 65,000 seconds (about 18 hours). The gain settings on the MCA were adjusted to push all  $\gamma$ -ray energies into the lower channels and clearly view the muon continuum at higher energies, as seen in Fig. 1.4. The spectrum from each end of the lab was then integrated upwards from channel 214, past the  $\gamma$ -ray peak, to encapsulate only muon counts. Results indicated that the muon background was lower at the east end.

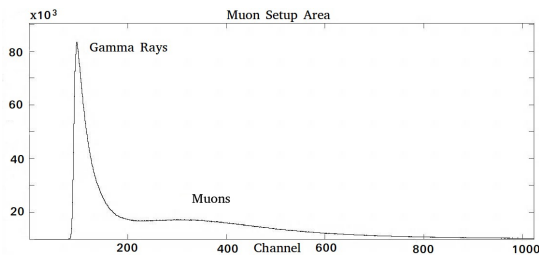


**Figure 1.4: Muon continuum with gain settings such that  $\gamma$  rays are pushed into one low-channel peak.**

Like muons, neutrons are produced in particle showers and are highly penetrating. After being scattered to lower energies, neutrons are commonly captured by nuclei, which then emit  $\gamma$  rays.

The neutron background was measured with a model IV inventory sample counter (INVS) which consisted of eighteen independent  $^3\text{He}$  tubes. The data from each tube populated a histogram of the type seen in Fig. 1.5. Then, a program was written which integrated all eighteen histograms over specified intervals to determine the total number of neutrons detected, with low-channel peaks consisting of  $\gamma$  rays being discarded.

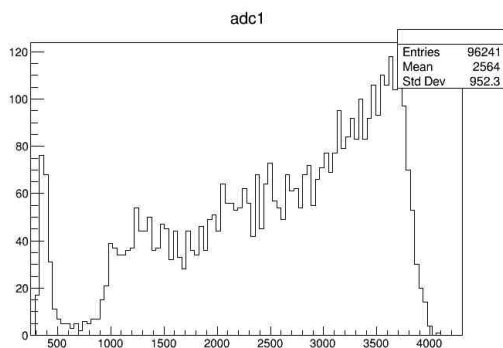


**Figure 1.5: Neutron spectrum from tube 1 at the west end of LENA. Each run produced 18 histograms of this type.**

The INVS counter was run for 24 hours at each location and measured more neutrons at the west end of LENA than at the east by a factor of greater than two.

An existing GEANT4 simulation of the INVS was used to derive the neutron flux at each end of LENA. From 50 keV up to 100 MeV, the neutron energy distribution exhibits a power law proportionality of the form  $N = E^{0.08}$ , where  $N$  is the number of neutrons and  $E$  is the energy [Roe98]. A 20m x 20m planar neutron source was created 10m above the detector which emitted neutrons according to this energy distribution in the  $-y$  direction (straight downward). Then, 300mm thick concrete walls were created which enclosed the volume containing the INVS.

Results are summarized in Table 1.1 and indicated that the simulation was over-counting slightly, leading to low calculated flux values [Cav15]. However, the simulated distribution of counts across the 18 tubes of the INVS approached the experimental distribution.

**Table 1.1: Calculated neutron flux values based on GEANT4 simulation.**

Location	Neutron Flux
Actual Neutron Flux at Sea Level	$5.5 \times 10^6 \text{ m}^2/\text{d}$
Calculated Flux (West End)	$1.79 \times 10^6 \text{ m}^2/\text{d}$
Calculated Flux (East End)	$7.57 \times 10^5 \text{ m}^2/\text{d}$

There are three floors in the building above the east end of LENA, but the west end is only shielded by its ceiling. This structural shielding is enough to make the background from cosmogenic particles at the east end significantly lower than at the west end. Despite the higher environmental  $\gamma$ -ray background, the target in LENA should remain in its current location at the east end of the lab, where the muon and neutron backgrounds are lower.

[Cav15] F. Cavanna and P. Prati, 2015, <https://slideplayer.com/slide/12536177/>.

[Heu95] G. Heusser, *Ann. Rev. Nucl. Part. Sci.*, **45**, 543 (1995).

[Lon06] R. Longland *et al.*, *Nucl. Instrum. Methods A*, **566**, 452 (2006).

[Roe98] S. Roesler, W. Heinrich, and H. Schraube, *Adv. Space Res.*, **21**, 1717 (1998).

### 1.3 Studying the Response of a Cerium Bromide Scintillator for Nuclear Structure Studies at HI $\gamma$ S

S.R. JOHNSON, *Boise State University*; R.V.F. JANSSENS, M.D. JONES, D.R. LITTLE, *TUNL*

Nuclei with a "magic number" of protons and/or neutrons are especially stable. Nuclear resonance fluorescence (NRF) experiments utilizing Lanthanum Bromide (LaBr<sub>3</sub>) detectors are underway at the High Intensity Gamma-Ray Source (HI $\gamma$ S) facility to better understand the structure of these magic nuclei. LaBr<sub>3</sub> detectors have good energy and timing resolution, but also have an intrinsic gamma-ray background which can mask data in some lower-energy experiments at HI $\gamma$ S. We would like to determine whether Cerium Bromide (CeBr<sub>3</sub>) detectors will be useful for these studies at HI $\gamma$ S in the place of LaBr<sub>3</sub> detectors. CeBr<sub>3</sub> detectors have been examined to determine their energy resolution as a function of supplied voltage at different energy levels. Coincidence timing resolution was also measured. At a later date, similar measurements will be taken of a LaBr<sub>3</sub> detector for a direct comparison. We expect CeBr<sub>3</sub> to have similar energy and timing resolution to LaBr<sub>3</sub> with low background radiation which may provide a new level of sensitivity in experiments at HI $\gamma$ S studying the structure of nuclei.

NRF experiments require the ability to detect photons at different angles in order to determine the energy states of nuclei being excited by a beam of polarized photons. Nuclear structure studies at HI $\gamma$ S use high-purity germanium (HPGe) detectors along with LaBr<sub>3</sub> detectors in these NRF experiments. HPGe detectors are known for their excellent energy resolution (about 1.8 keV at 1MeV). LaBr<sub>3</sub> detectors have good timing resolution and higher efficiencies which serve to complement HPGe's good energy resolution. If it can be shown that CeBr<sub>3</sub> has resolutions comparable to LaBr<sub>3</sub>, it may be a useful replacement for LaBr<sub>3</sub> detectors in future studies, eliminating the background radiation at 1436 keV that contaminates spectra when LaBr<sub>3</sub> detectors are in use.

Two separate CeBr<sub>3</sub> detectors were examined in order to characterize the response of this type of scintillating crystal. The detectors have the same crystal size (2" by 2") so their properties should be comparable. One detector takes positive high voltage to power its photomultiplier tube while the other takes negative high voltage, so they are referred to as the "positive polarity" and "negative polarity" detectors, respectively.

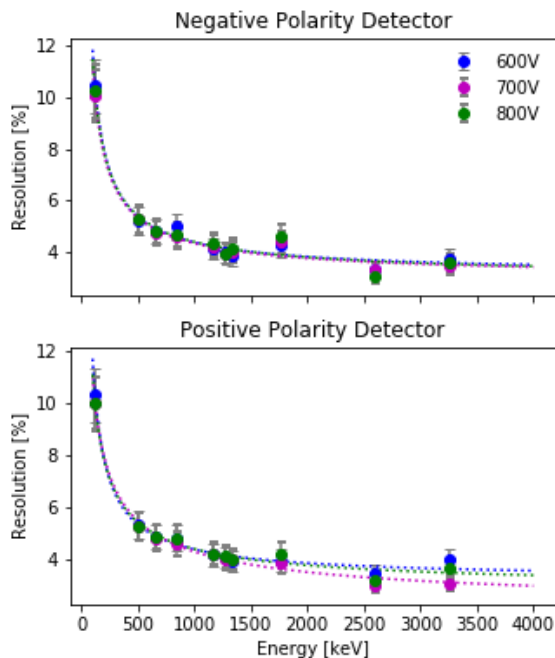
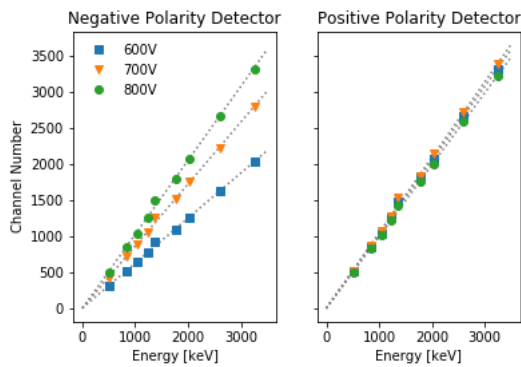


Figure 1.6: Energy resolution percentages are plotted for each CeBr<sub>3</sub> detector at operating voltages of 600V, 700V, and 800V. The error shown is an estimated 10 percent systematic uncertainty.

The CeBr<sub>3</sub> detectors were used to take spectra of

a handful of radioactive sources ( $^{60}\text{Co}$ ,  $^{57}\text{Co}$ ,  $^{56}\text{Co}$ ,  $^{137}\text{Cs}$ , and  $^{22}\text{Na}$ ) with photopeaks at well-known energies ranging from 123 keV to 3254 keV. The operating range of both the positive and negative polarity detectors is around 600V to 800V. This range was explored in full when examining the energy resolution. Resolution was determined as a percentage by dividing the FWHM of a photopeak by its centroid. The operating voltage did not have much effect on energy resolution. The resolution curves in Figure 1.6 follow an inverse square root trend with resolution worsening at lower energies as expected and resolutions of about 4% at higher energies. The  $\text{CeBr}_3$  detectors behave linearly in energy, as shown in Figure 1.7.



**Figure 1.7:** The channel numbers of known peaks in the spectra of  $^{56}\text{Co}$  were identified and plotted against the energies of said peaks. The slope of the line for each run depends only on the gain settings on the amplifier which were changed from run to run in order to include the entirety of the  $^{56}\text{Co}$  spectrum.

Coincidence timing measurements were taken using  $^{60}\text{Co}$  which decays producing  $\gamma$ - $\gamma$  coincidences at energies of 1173 keV and 1333 keV. With the positive and negative polarity detectors positioned at 180 degrees with respect to one another and the  $^{60}\text{Co}$  source in the middle, both scintillators should detect 1173 keV and 1333 keV photons at the same time. The detectors have two outputs; a timing pulse and an energy pulse. The timing output of one detector is

delayed by a set length of time, then both pulses are sent through a time-to-amplitude converter that outputs a pulse of a height proportional to the length of time between which it received signals from the start (signal with no delay) and stop (delayed signal) inputs. This time-to-amplitude signal feeds into an analog-to-digital converter which creates a timing histogram where we should see a peak at the time corresponding to the set delay. By applying delays at a range of different times we were able to calibrate the time spectra and determine the width of a channel. The FWHM of the time spectra were then found and quoted as timing resolution. Figure 1.8 shows the results of these measurements.

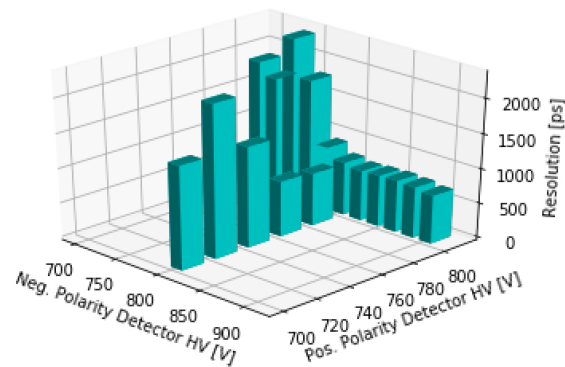


**Figure 1.8:** FWHM timing resolution worsens when the detectors are operating at lower voltages. The best resolution obtained by adjusting settings was around 700 ps.

This project sought to increase the sensitivity in nuclear structure studies by looking into a new type of detector for future use. The measurements described here for  $\text{CeBr}_3$  will be repeated with a  $\text{LaBr}_3$  detector. This will allow for a direct comparison of energy and timing resolution in  $\text{LaBr}_3$  and  $\text{CeBr}_3$ . The background spectra will also be compared in both types of detectors. It is expected that the  $\text{CeBr}_3$  detector's background levels will be much lower than those of  $\text{LaBr}_3$  due to Ce being stable.,  $\text{CeBr}_3$  may be a useful replacement for  $\text{LaBr}_3$  in these studies of magic nuclei.

## 1.4 Construction of a Wire Chamber for Reactor Neutrino Studies

H.C. HASAN, *The Ohio State University, Columbus, OH*; C.M. AWE, *TUNL*

Neutrino interactions can be used as a probe for exploring physics beyond the Standard Model. However, the rarity of neutrino interactions and presence of high backgrounds make detection difficult. We wish to construct a time projection chamber (TPC) capable of reconstructing the kinematics of an inverse beta decay event. The TPC will detect the products of inverse beta decay using isobutane as a target material. As isobutane is not a well-characterized gas, we have constructed a wire chamber to study quenching factors in isobutane. We first studied the wire chambers response for known sources, obtaining a muon spectrum using P-10 gas as a target. In the future, we will use the wire chamber to characterize isobutane for use in the TPC. Additionally, we possess a commercially bought wire chamber filled with an unknown target gas, and wish to calibrate it. We have created a GEANT4 simulation package for calibrations.

Neutrinos are considered a powerful tool for exploring beyond-Standard Model physics. Additionally, their tendency not to interact with matter means that they can be traced back to their source. Thus it is desirable to construct a detector sensitive to the direction of an incident neutrino. Aside from pure physics interest, such a detector may have applications in nuclear security; tracing neutrinos may allow identification of potential nuclear reactors. It is well-known that neutrinos can be detected using inverse beta decay, an interaction in which an electron antineutrino scatters off a proton and creates a neutron and positron ( $\bar{\nu}_e + p \rightarrow n + e^+$ ). Post-interaction, the neutron undergoes scattering in the medium to create ionization at discrete points along its track, while the positron causes ionization continuously. A time projection chamber (TPC) uses the resulting ionization to extract kinematic information about the two product particles and reconstruct the direction of the incident neutrino. It is advantageous to use hydrogenated material as a target, as inverse beta decay becomes a two-body problem. It is our intent to use isobutane ( $C_4H_{10}$ ) as a target material in the TPC, as it possesses a high hydrogen content but fewer risks than pure hydrogen. Prior to this, however, we must study quenching factors for neutron recoils in isobutane. In this project, we are developing a wire chamber to be used for this purpose [Awe18].

Prior to using the wire chamber for studying isobutane, we study its response for known sources. In an attempt to obtain a spectrum, the wire chamber was initially filled with nitrogen and tested with a  $^{55}Fe$  source. Upon failing to obtain a  $^{55}Fe$  spectrum,

it was tested with  $^{137}Cs$ . As the detector's response indicated a possibility of sparking at a high-voltage connection, the chamber was disassembled, its connection re-soldered, and reassembled. After further attempts at obtaining a spectrum in nitrogen were unsuccessful, the wire chamber was filled with P-10 gas (90% argon, 10% methane) to again attempt to obtain a  $^{137}Cs$  spectrum. These attempts were also unsuccessful.

To identify potential faults in the chamber, a muon hodoscope was used as an external data acquisition trigger in order to obtain an atmospheric muon spectrum. Monitoring muon data over three consecutive days allowed us to conclude that the chamber was leaking, as shown in Fig. 1.9.

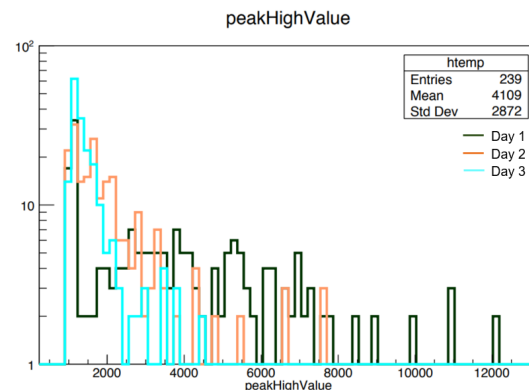


Figure 1.9: Depicted are atmospheric muon spectra taken over the course of three consecutive days, indicating a leak in the chamber.

A leak in the chamber was identified and sealed, and additional data was collected using the hodoscope. This data is depicted below in Figs. 1.10 and 1.11:

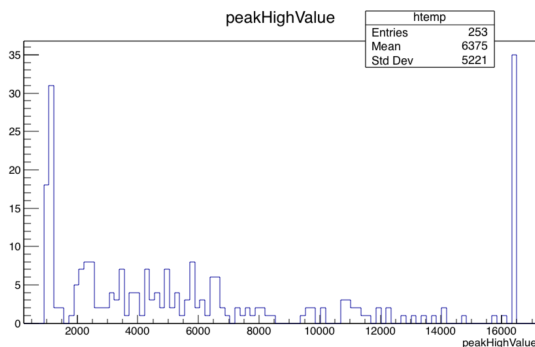


Figure 1.10: Initial observed muon spectrum after sealing the leak.

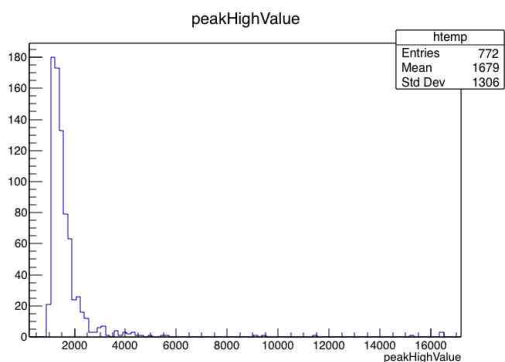


Figure 1.11: Muon data recorded subsequently.

The inconsistency in recorded data between runs indicates remaining faults in the wire chamber. Further leak checking and other fault inspections are ongoing.

We have in our possession a second, commercial wire chamber. This chamber is sealed, unmarked, and filled with either boron trifluoride ( $\text{BF}_3$ ) or  $^3\text{He}$ . In order to calibrate this chamber to gamma-ray sources, a GEANT4 simulation package, called WIRECHAMBERSIM, has been created.

WIRECHAMBERSIM simulates the commercial

wire chamber and evaluates the amount of energy deposited by incident gamma rays. WIRECHAMBERSIM is capable of simulating both  $\text{BF}_3$  and  $^3\text{He}$  as the target material in the chamber, and simulating other particles with minimal edits. Of most use is WIRECHAMBERSIM's associated shell script, dubbed `GammaEnergyScan.sh`, which performs many trials of varying gamma ray energy. This script will be used to calibrate the wire chamber to gamma ray sources.

Fig. 1.12 below shows the energy deposited by gamma rays of varying energy in a chamber filled with  $^3\text{He}$ . Each gamma ray energy value was simulated many times to account for statistical variations. All energies are in keV.

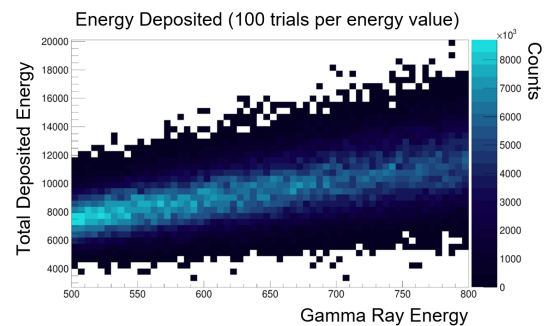


Figure 1.12: Energy deposited by gamma rays in the target gas of the simulated wire chamber.  $^3\text{He}$  was used as the target gas in this run.

Work on the lab-assembled wire chamber remains ongoing. After leaks and other faults are eliminated, the wire chamber will be calibrated. The chamber will then be used to study quenching factors for nuclear recoils in isobutane, in order to use isobutane as a target material for a TPC. The commercial wire chamber will be calibrated from Monte Carlo simulations using `GammaEnergyScan.sh` in conjunction with WIRECHAMBERSIM. It will then be placed in a thermal neutron bath to obtain a neutron capture spectrum, whereupon the target gas may be identified.

---

[Awe18] C. Awe, *A Time Projection Chamber for Reactor Neutrino Studies*, 2018.

## 1.5 Characterizing NaI[Tl] Scintillating Crystals for the COHERENT Experiment

J.S. DEVANEY, *Indiana University Bloomington, Bloomington, IN*

COHERENT is seeking to observe coherent elastic neutrino-nucleus scattering (CEvNS) using a variety of detectors. To show the  $N^2$  scaling of the CEvNS cross section with neutron number, COHERENT is deploying detectors with different nuclei, including a multi-ton NaI[Tl] scintillating detector. To prepare for this deployment, individual NaI[Tl] crystals need to be characterized by their non-linear light response at low energies. Four low-energy gamma-ray sources were used to calibrate the detector between 20 and 1500 keV. As a result of the calibration, energy resolution of the detector was measured as a function of energy in the crystals, and this data was parameterized and fit. The fit was used in the output of simulations to compare to source data. Lastly, a new pulse shape discrimination algorithm aided in the identification of noise and abnormal pulses present in the detector.

Despite coherent elastic neutrino-nucleus scattering having a large cross section compared to other low-energy neutrino cross sections, the nuclear recoils generated by the reaction have low energies which makes them difficult to observe. COHERENT is planning to deploy a multi-ton NaI[Tl] detector, but before this is done the individual crystals must be characterized. In this project, the crystals were characterized by performing energy calibration, analyzing detector resolution, and implementing pulse shape discrimination (PSD) on individual crystals.

For COHERENT, the energy deposited in the detectors is expected to be in the keV regime. NaI[Tl] is known to have a non-linear light response in this region of interest, and this is compounded by the fact that the nuclear recoil generated by CEvNS has a diminished ability to generate scintillation compared to electron recoils. It is necessary to accurately calibrate the detectors and understand the non-linearity of the light response to understand the signal expected from CEvNS interactions. To calibrate the NaI[Tl] detectors, four gamma-ray sources with well-known energy lines were used. A background run was taken prior to the source runs, and this was used to make background subtracted spectra to filter out background noise. Using these background subtracted spectra, the peaks of energy lines present in the spectra were fit using Gaussian functions.

In Fig. 1.13, data taken from the source runs was plotted and compared to previous data from Ref. [Kho10]. The non-linearity is clear, but there is another feature showing a dip in the light response

around 33.2 keV which is characteristic of the iodine k-shell binding energy. This is similarly present in Ref. [Kho10]. In the future, more data points at low energies would improve mapping of the non-linear response.

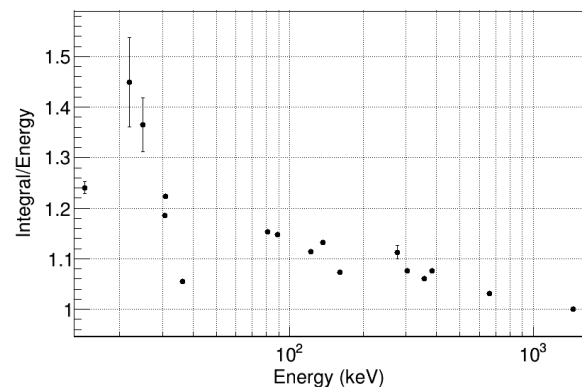


**Figure 1.13:** Relative light yield shown at various energies by using Gaussian fits of spectral energy lines. It is normalized by the 1460 keV line from  $^{40}\text{K}$ . Data points are from four gamma sources:  $^{133}\text{Ba}$ ,  $^{137}\text{Cs}$ ,  $^{57}\text{Co}$ , and  $^{109}\text{Cd}$ .

After mapping the non-linearity, detector resolution was plotted at various energies and compared with the resolution from another crystal [Kho10]. Both crystals show a similar decrease in resolution as the energy decreases. A three parameter fit was used, with the form given by Resolution =  $\sqrt{\alpha * x^2 + \beta * x + \gamma/x}$ . The best fit parameter values were  $\alpha = 1.5298 \times 10^{-3}$ ,  $\beta = 1.8606$ , and

$\gamma = 1.9329 \times 10^{-7}$ . The fit was used to apply realistic energy resolution to detector simulations, which will help refine energy calibration and resolution. There are a number of unknown features present in both simulation and source data, and applying this resolution to the simulations will help to understand the detector response to these sources.

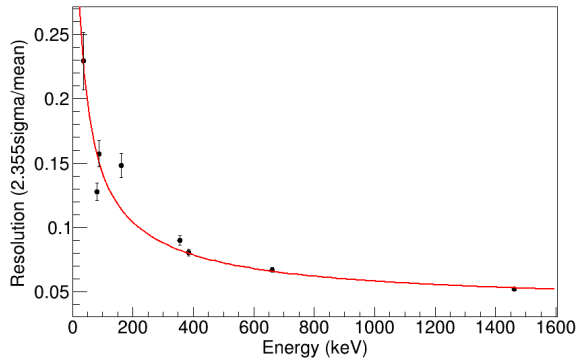


**Figure 1.14: Resolution data taken from the Gaussian fits of spectral energy lines. Errors come from the sigma fit. The fit in red used three parameters.**

Lastly, a new PSD algorithm from Ref. [Che14] was used to sort and filter out noise and abnormal pulses. The parameter  $\tau$  weights the pulses based on the geometry of the rise and decay time of the pulse, so that pulses with different shapes appear in different positions in the histograms. This weighting allows us identify noise and abnormal pulses in the spectra. Five regions were highlighted to understand the types of pulses present in the different regions. Region 1 is where pulses free from any abnormal noise were seen. Regions 2 and 3 has pulses showing pile-up. Regions 4 and 5 showed pulse pile-up, but with thin pulses possibly due to PMT Noise. PSD is a powerful tool to remove unwanted noise from the source runs, but

before they are removed, their effect on the data will be considered.

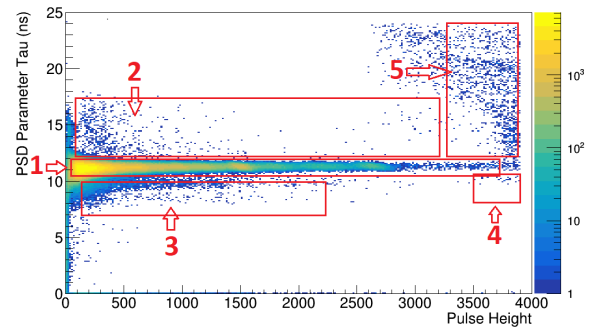


**Figure 1.15: PSD Algorithm  $\tau$  from Ref. [Che14] was used to sort and filter for noise and abnormal pulses within our data. The different regions labeled are characteristic of different types of pulses.**

In conclusion, individual NaI[Tl] crystals were characterized and energy calibration was performed. The resolution function was applied to simulations to compare to source data. Lastly, a new PSD algorithm was implemented to aid in sorting out different types of pulses. Future work includes acquiring more low-energy data points to improve the non-linear light response mapping around iodine k-edge. Once the effect of PSD cuts on the data is understood, the PSD algorithm could be implemented to improve the signal-to-noise ratio in the spectra. Finally, temperature-dependent and geometric effects will be tested.

[Che14] J. Cherwinka *et al.*, Phys. Rev. D, **90**, 092005 (2014).

[Kho10] I. V. Khodyuk, P. A. Rodnyi, and P. Dorenbos, J. Appl. Phys., **107**, 113513 (2010).

## 1.6 Event Generator for Neutrinos on Deuterons

J. KOROS *Florida State University, Tallahassee, FL*; K. SCHOLBERG *Duke University, Durham, NC*

Studies of coherent elastic neutrino-nucleus scattering (CEvNS) at the Spallation Neutron Source (SNS) are currently limited by uncertainties in the neutrino flux. A heavy water detector has been proposed to reduce these uncertainties by measuring the neutrino flux. Simulations of such a detector required the creation of an event generator for the  $\nu_e + d \rightarrow e^- + p + p$  reaction. The cross sections over a range of energies for the detection of an electron were weighted by the SNS flux to give a realistic representation of reactions for input into a Monte-Carlo simulation. The code written to create these distributions is available for application to similar projects.

COHERENT is a collaboration studying CEvNS, a process with a well predicted but very small cross section. Several detectors are operated at the SNS at Oak Ridge National Laboratory to study CEvNS. Currently there is around 10% uncertainty in SNS neutrino flux. In order to reduce this uncertainty and therefore improve measurement of CEvNS, a heavy water detector is planned to measure the neutrino flux. Monte Carlo simulations will be done to determine the best design of this detector. To perform these simulations, it is necessary to create an event generator for neutrinos on deuterons to give event information.

The reaction that will be used to measure flux is  $\nu_e + d \rightarrow e^- + p + p$ , where the electrons are the detected particles. This reaction has been studied and theoretical calculations for these cross sections are available online [Nak01]. Using Python's Beautiful Soup library, a web scraper was written to download these cross-section tables into readable text files.

While the Gudkov cross-section tables give the double differential cross section with respect to electron momentum and solid angle, histograms for the event generator were constructed with even bins in electron energy and  $\cos\theta$ . This made the change of variables described in Eqn. 1.3 necessary.

Because the tables covered a wide range of neutrino energies and had irregular intervals, a TH2Poly histogram was first constructed. The TH2Poly class in ROOT allows the user to define bins of any size and shape, so this method ensured all bins were correctly filled. A regularly binned TH2D histogram was then filled from each TH2Poly, and linear interpolation was used where multiple TH2D bins fell inside a single TH2Poly bin. Fig. 1.16 illustrates this.

$$\begin{aligned} \frac{d^2\sigma}{dE_e d\cos\theta} &= \left(\frac{dp_e}{dE_e}\right) \left(\frac{d\Omega_e}{d\cos\theta}\right) \frac{d^2\sigma}{dp_e d\Omega_e} \\ &= \left(\frac{E_e}{\sqrt{E_e^2 - m_e^2}}\right) \left(\frac{\sin\theta d\theta \int_0^{2\pi} d\phi}{d\cos\theta}\right) \frac{d^2\sigma}{dp_e d\Omega_e} \\ &= \left(\frac{E_e}{p_e}\right) (2\pi) \frac{d^2\sigma}{dp_e d\Omega_e} \end{aligned} \quad (1.3)$$

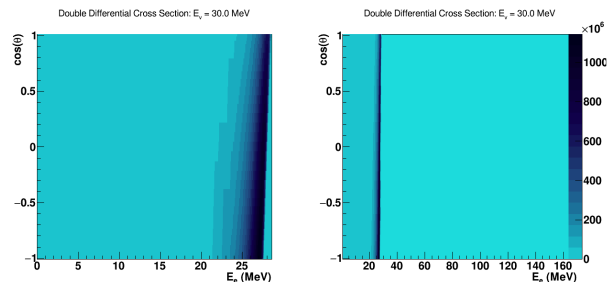


Figure 1.16: Left, TH2Poly; Right, TH2D

The tables gave cross-section information for neutrino energies from 1.5 MeV to 170 MeV, which is an adequate range for the SNS flux, but for larger energies there are also sizable gaps between calculated tables. To improve this resolution, interpolated histograms were created every 0.1 MeV using a linear interpolation algorithm that compared variably selected bins from the existing histograms. Fig. 1.17 shows an example of these interpolated histograms.

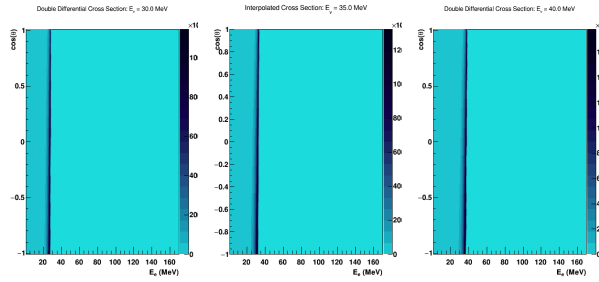


Figure 1.17: Left, 30 MeV; Center, Interpolated 35 MeV; Right, 40 MeV

A single TH2D histogram was created by weighting the cross section histograms over all neutrino energies to the SNS flux. Eqn. 1.4 gives the equation used to weight each bin. Fig. 1.18 shows the SNS flux distribution, and Fig. 1.19 shows this final flux-weighted histogram.

$$\sum_{E_\nu} \left( \frac{d^2\sigma}{dE_e d\cos\theta} \right)_{E_\nu} (\Phi)_{E_\nu} \left( \frac{\text{binsize}}{\text{max}} \right)_{E_\nu} \quad (1.4)$$

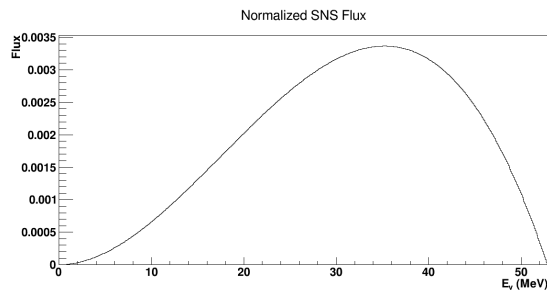


Figure 1.18: Normalized  $\nu_e$  SNS flux distribution

The output of the event generator is a list of elec-

tron event information. This process involves randomly sampling from the flux-weighted 2D histogram and outputting electron energy and  $\cos\theta$  for each of these sampled events.

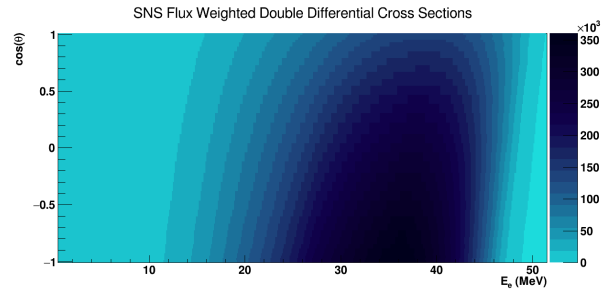


Figure 1.19: Flux-weighted distribution

The total flux weighted cross section is a useful number to know, and is also a good check of this process. Assuming everything has been done correctly, obtaining this number is as simple as integrating over the final 2D flux-weighted histogram. Doing this integral gives a flux weighted cross section of  $1.056 * 10^{-43} \text{ cm}^2$ . The Gudkov tables also provide calculated total cross sections by neutrino energy, so weighting these using the SNS flux should produce the same value. Performing this calculation gives a cross section of  $1.043 * 10^{-43} \text{ cm}^2$ . Error propagation on this integral is unnecessary for event generation, but these two values agree reasonably well.

All code written for this project is available at: <https://github.com/jkoros/event-generator>

[Nak01] Nakamura *et al.*, Tables of Neutrino (Anti-Neutrino) Deuteron Reactions Cross Sections, (2001), <http://boson.physics.sc.edu/~gudkov/NU-D-NSGK/Netal/index.html>.

## 1.7 Ionization Chamber Development for the Detection of Tritium

K. PARHAM, *Hendrix College, Conway, AR*; C. MALONE, C.R. HOWELL, *TUNL*

An experiment to measure the kinematically-complete cross section of the photodisintegration of the triton is planned at the High Intensity  $\gamma$ -ray Source (HI $\gamma$ S) facility in order to test current models of three-nucleon interactions. Because tritium is a radioactive material, precautions must be taken during transport of the target system to avoid leaks to the environment. A safety system made up of four ionization chambers was built in order to monitor the intermediate containment chamber for tritium leaks. Two ionization chambers are open in order to monitor for tritium while the remaining two chambers are sealed for background subtraction. All ionization chambers will operate in air and will be battery powered for mobility.  $^{90}\text{Sr}$  and  $^{241}\text{Am}$  were used to test the ionization chambers. When exposed to the  $^{241}\text{Am}$  source, the open detectors displayed a significant gain. A similar gain is expected should the tritium target leak during transport.

Three-nucleon interactions (3NI) are important to the understanding of nuclear structure and nuclear reactions. Current two-nucleon interaction models fail to correctly predict the behavior in some three-nucleon systems [Glö96]. The inclusion of 3NI is required to accurately fit reported data, in particular the binding energies of  $^3\text{H}$  and  $^3\text{He}$ . One sensitive method of assessing the validity of 3NI models is by measuring the neutron-neutron scattering length ( $a_{nn}$ ) in certain kinematic configurations. To this end, an experiment is planned at the HI $\gamma$ S facility to measure the cross section of the kinematically-complete three-body photodisintegration of the triton. In this experiment,  $a_{nn}$  will be extracted from the measured cross sections. The experiment requires a tritium gas target to be transported between buildings at TUNL and, due to regulations concerning tritium, an ionization chamber system is needed to monitor the intermediate containment chamber for any leaks during transport. While commercial tritium monitors are available, the constructed system is smaller, lighter, and offers more diagnostic information. If there were a signal indicating a tritium leak, the leak could be confirmed by checking the current on each ionization chamber, reducing false positives.

Four ionization chambers were constructed with aluminum shells that were 6 in. long, 1.125 in. diameter, and 0.014 in. thick. Each ionization chamber has two end caps of the interior shell diameter that were 0.625 in. deep. A 100 micron copper wire was soldered to a BNC connector at one end and through

the opposite endcap. The exposed wire on the opposite end was sealed with epoxy. Two of the ionization chambers have six holes drilled through the endcaps, each of 0.188 in. diameter. These chambers will rely on diffusion rather than active pumping to detect any tritium leaks. The remaining two ionization chambers were sealed and will be used for background subtraction.



Figure 1.20: A cross sectional view of an open detector

Tritium emits electrons with an average energy of 5.7 keV, which travel about 0.3 cm in air. Tritium could not be used to test the ionization chambers due to resulting contamination. Instead, the ionization chambers were tested using  $^{90}\text{Sr}$  (an electron source) and  $^{241}\text{Am}$  (an  $\alpha$  source). It was necessary

to use sources which produced higher energy particles that travel further because, unlike the tritium gas that will diffuse inside of the ionization chambers, the sources needed to remain outside of the chambers. The sources were placed in front of each detector and the current on the central wire was read off of an electrometer in the picoamp range and recorded. The electrons emitted by  $^{90}\text{Sr}$  have an average energy of 0.2 MeV and travel about 20 cm. When the  $^{90}\text{Sr}$  source was used, background fluctuations in current exceeded the signal from the source. The fluctuations were caused by capacitance changes due to nearby materials and air flow through the room. These changes in capacitance are not expected to be present when the ionization chambers are in use.

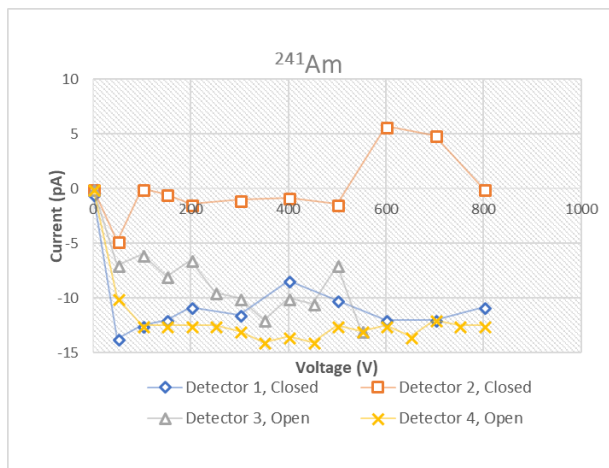


Figure 1.21: Current read from detectors when the  $^{241}\text{Am}$  source was introduced

The  $^{241}\text{Am}$  source emits  $\alpha$  particles with an aver-

age energy of 5.5 MeV that travel about 4.5 cm. Although fluctuations in the current were still present, this source produced a significant signal on the open detectors. It also appeared to produce a signal on one of the sealed detectors (Detector 1).

Finally, measurements were taken using a background subtraction method. An open and closed detector were held at opposite polarities to correct for backgrounds. The currents were added and the voltage of the sealed detector was adjusted until the current read zero. The  $^{241}\text{Am}$  source was used once again and the resulting signal was significantly more stable than in measurements taken without background subtraction.

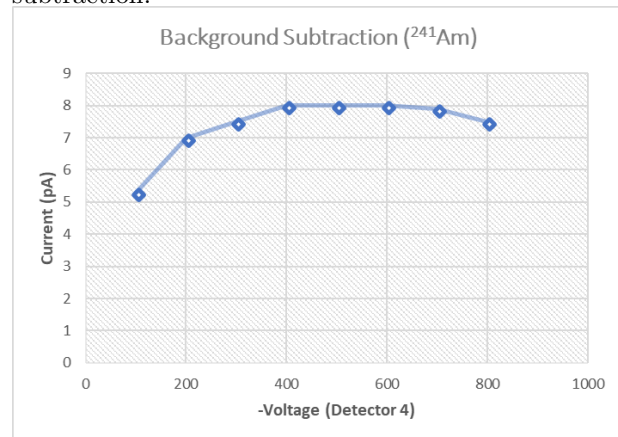


Figure 1.22: Electrometer current after background subtraction (using detectors 2 and 4) when the  $^{241}\text{Am}$  source was introduced

[Glö96] W. Glöckle *et al.*, Phys. Rep., **274**, 107 (1996).

---

## 1.8 Development of a Rutherford Backscattering Spectrometry Station for TUNL

---

A. WANTZ, *Indiana Wesleyan University, Marion, IN*; R. LONGLAND, *TUNL*

**Rutherford backscattering spectrometry (RBS) is a technique used to characterize solids via surface-layer analysis. RBS is performed at TUNL to better understand the targets that are used in experiments. The RBS chamber located at TUNL was upgraded by increasing the number of detectors and improving the vacuum. The baseline vacuum was reduced from 2E-5 to 7E-7 torr. The number of detectors was increased from one to four to allow for better characterization of complicated targets. These were integrated into the existing data analysis system. Silicon dioxide targets were produced and RBS analysis was performed. The RBS data was fit with SIMNRA software. The experimental cross section was compared to the theoretical cross section given by the Rutherford formula. Our preliminary results show good agreement between the two.**

Much of nuclear physics focuses on finding the probability of a given reaction occurring, the cross section for the reaction. To calculate these cross sections, it is imperative to know details about the target one is using, since both the number of reactions that do occur and the number of potential reactions that could occur must be known. Often, targets are acquired from outside sources with some amount of uncertainty in the composition or thickness. RBS is an analytical technique that is particularly suited to the task of evaluating these targets. The goal of this project was to improve the efficiency and effectiveness of the RBS station at TUNL and to test the setup by measuring scattering cross sections off of silicon dioxide (SiO<sub>2</sub>).

To prepare for the experiment, a number of steps were taken. First, the chamber and beamline were leak-checked using a helium leak chaser in order to identify the leaks responsible for the barely adequate vacuum. Many small leaks were identified. To fix them, the ports into the chamber were taken off, cleaned, and had their O-rings cleaned or replaced. A major leak was found underneath the ionization suppressor where the epoxy seal had worn away. This area was covered with vacuum-grade epoxy, and the vacuum improved dramatically. After the chamber was pumped on for a couple weeks, the baseline vacuum improved from 2.3E-5 torr to 7.0E-7 torr. After a final leak chase, no leaks were found.

Secondly, silicon detectors were installed at 150, 134, and 119 degrees, in addition to the detector already situated at 165 degrees. These detectors were

wired with high voltage and signal processing cables. The high voltage control system, the Experimental Physics and Industrial Control System (EPICS), was set up for the single detector at 165 degrees. This was expanded to control all four detectors, giving the ability to set and read the voltage and to read the leakage current. The high voltage of the detectors was adjusted to make the gain approximately equal.

Silicon dioxide targets were made in order to test the improved chamber. These were made by floating a 40 microgram carbon foil onto a metal frame. Then silicon dioxide powder was placed in a tantalum boat and evaporated onto the carbon foils. The thickness of silicon dioxide was measured by a thickness monitor. Two targets were made in this manner.

The experiment was conducted on the 52 degree beamline, with the alpha particles accelerated through the 10 MV Tandem Van de Graaf generator. A 2 MeV <sup>4</sup>He beam was incident on a ladder consisting of targets including a gold foil on carbon and the two silicon dioxide targets. Data was collected for roughly 30 minutes per target. The integrated beam current on target was recorded for each run. This was used to calculate the number of beam particles in the experiment.

The data was analyzed to determine if the scattering was Rutherford in nature, given by the formula,

$$\frac{d\sigma}{d\Omega} = \left( \frac{Z_1 Z_2 e^2}{4E_0} \right)^2 \frac{1}{\sin^4(\theta/2)},$$

with  $Z_1$  and  $Z_2$  representing the atomic number of the beam nuclei and target nuclei respectively,  $E_0$

representing the energy of the beam, and  $\theta$  the scattering angle. To assist in this determination, a plot was created in ROOT (via a C++ script) to show the theoretical differential cross section, which is shown as the red line in Figure 1.

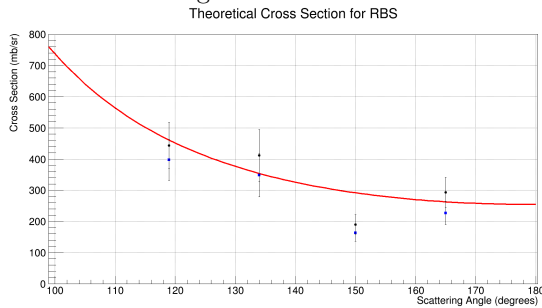


**Figure 1.23:** Depicted is the theoretical cross section for alpha particles backscattering off silicon (red line). The blue points are the experimental cross sections calculated from the first SiO<sub>2</sub> target, while the black points show those of the second SiO<sub>2</sub> target.

The experimental differential cross section was calculated with the cross section formula, given by

$$\frac{d\sigma}{d\Omega} = \frac{A * N_R}{N_T * N_B * \Omega},$$

with  $A$  being the area of the beamspot,  $N_R$  the number of reactions of interest (alpha particles scattering off silicon),  $N_T$  the number of target nuclei,  $N_B$  the number of beam particles, and  $\Omega$  the solid angle of the detector. To obtain  $N_B * \Omega$ , we used SIMNRA, a simulated ion beam software to fit the peaks. We first used an energy calibration target (gold on a carbon foil) to find the relationship between the channel number and the energy. From there, we used the energy calibration to find the parameters for the SiO<sub>2</sub> targets that were made. Although we had approximate measures of the thickness of the SiO<sub>2</sub> layer from the thickness monitor, we needed to check if this was an accurate measurement. Our spectra also showed an unexpected peak due to evaporated tantalum in the boat that held the SiO<sub>2</sub>. This was included into the simulated target. After fitting the relevant parameters (a sample is shown in Figure 2), the num-

ber of beam particles/sr was extracted and used in the experimental cross-section formula.

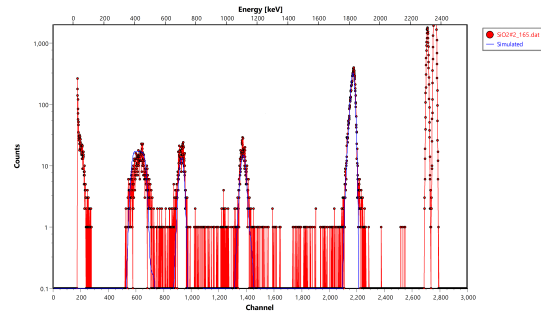


**Figure 1.24:** Shown here is a sample SIMNRA spectrum for a SiO<sub>2</sub> target. From left to right, the fitted peaks correspond to carbon, oxygen, silicon, and tantalum. The software was used to obtain the number of target nuclei and number of beam particles for the experimental differential cross-section calculation.

The error bars on the data in Figure 1 were calculated based on propagation of error for each quantity in the experimental differential cross section equation, with the largest source of uncertainty being the uncertainty of the number of beam nuclei (the peak height in SIMNRA). For the 134° detector, the carbon did not show up in the energy calibration spectrum, so there was greater uncertainty in the number of beam nuclei, which accordingly increased the size of the error bars. We believe that the reason that the 150° cross section point shows disagreement is that there may be dead regions on the silicon detector, which reduced the calculated cross section.

The goal of the project was to improve the RBS station; this goal was accomplished. The enhanced vacuum makes the system more efficient, since it takes less time to pump down the chamber. The additional detectors provide more data on complicated targets.

The calculated cross sections lie along the theoretical curve, demonstrating that the scattering was indeed Rutherford. This agreement shows that the chamber is performing satisfactorily and accurately analyzing targets. The RBS station can be used to analyze targets more effectively going forward.

## 1.9 Application of Fourier Analysis to SQUID Systems in the nEDM EXPERIMENT

P.W. GIFFIN, *University of Kansas, Lawrence, KS*; R. GOLUB, A. DIPERT, *TUNL*

The physics of the neutron electric dipole moment (nEDM) has been discussed for more than half a century. The existence of the nEDM would be a confirmation of both parity and time reversal symmetry violation, thus providing evidence of "new physics". The standard model predicts that the neutron electric dipole moment is less than  $10^{-32}$  e cm. Current technology is not capable of measuring electric dipole moments this small. Fortunately, the  $^3\text{He}$ -UCN experiment will be able to detect electric dipole moments at the level of  $10^{-27}$  e cm, providing an unprecedented precision. Detection of such a small electric dipole moment requires detectors that are very sensitive which makes them susceptible to noise over their power supply. In this work, we have carried out a Fourier analysis and determined that noise exceeding frequencies of approximately 2 MHz would be sufficiently dampened by an optical fiber system.

The search for the neutron electric dipole moment (nEDM) is considered one of the best places to look for physics beyond the standard model. Current theory predicts that the nEDM is between  $10^{-40}$  and  $10^{-32}$  e cm. Although current technology is not capable of measuring with this level of precision, several experiments are being developed to improve the precision of nEDM measurements by nearly eight orders of magnitude [Lam09].

The  $^3\text{He}$ -UCN experiment aims to measure the nEDM using neutrons and  $^3\text{He}$  atoms undergoing angular precession about an applied electric field [Gol17]. A superconducting quantum interference device (SQUID) is capable of measuring the very small magnetic fields generated by this phenomenon. However, the SQUID is a very small device and requires supercooling in order to operate properly. Because of this, the SQUID is very sensitive to current and must be electrically isolated from its power supply.

An optical fiber system was purchased in order to accomplish this goal, but it was not clear what frequencies the system would filter out. Fig. 1.25 and Fig. 1.26 show that signals with frequencies above 2 MHz will be significantly dampened by the optical fiber system and filter out any unwanted noise.

Circuits involving resistors, capacitors, and inductors are often modeled by linear differential equations. These linear circuits can be treated as linear operators to an applied voltage.

When a small pulse is applied to a linear circuit,

it can be approximated as a delta function,  $\delta(t)$ , with a linear operator acting on it. The delta function is described by the properties

$$\delta(t) = \begin{cases} +\infty, & t = 0 \\ 0, & t \neq 0 \end{cases}$$

and

$$\int_{-\infty}^{+\infty} \delta(t) dt = 1.$$

The circuit will then transform the delta function into a form of Green's function. A Fourier transform of the form

$$\hat{f}(\omega) = \int_{-\infty}^{+\infty} f(t) e^{2\pi i \omega t} dt$$

can then be applied to the resulting signal. This function transforms a signal that was initially in the time domain into the frequency domain. When the signal is transformed into the frequency domain it will show which frequencies make up the signal as well as their magnitude and relative phase shifts.

This information is used to create gain and phase plots of circuits. The gain plot can be described by

$$\text{Gain} = 20 \cdot \log \frac{V_{out}}{V_{in}},$$

where  $V_{out}$  is the amplitude of the output voltage and  $V_{in}$  is the amplitude of the input voltage. The phase plot describes the relative phase shifts of the output and input signal.

In order to produce gain and phase plots of the optical fiber system, a small pulse lasting 80 ns was passed through the circuit. Using Igor Pro, a Fast Fourier Transform was performed on the resulting signal.

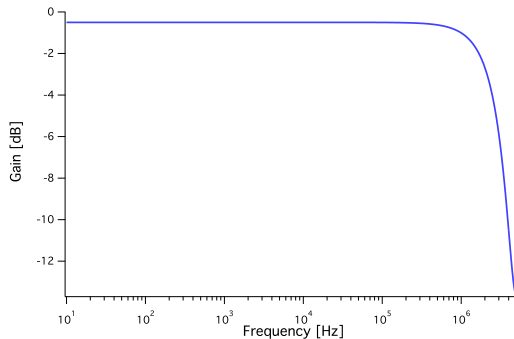


**Figure 1.25:** Depicted is a plot of the gain of the RF optical system as a function of frequency obtained using Fourier analysis.

This process generated 1250 sets of points at 4000 Hz intervals for both the gain and phase plots. Fig. 1.25 depicts the gain of the circuit as a function of frequency and Fig. 1.26 depicts the phase shift of the circuit as a function of frequency.

After observing the gain and phase plots, it can be seen that the circuit maintains a high gain for frequencies below 2 MHz and drastically dampens frequencies above 2 MHz. The phase starts to shift

around 200 kHz; however, this will not effect the strength of the signal.

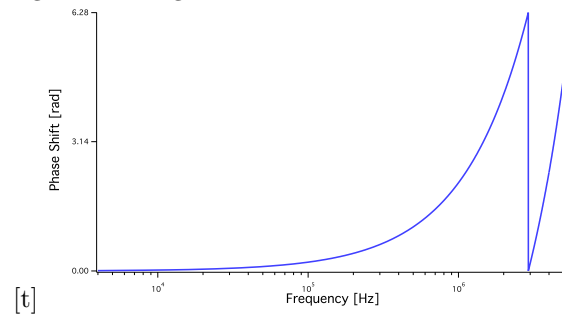


**Figure 1.26:** Depicted is a plot of the phase shift of the RF optical system as a function of frequency obtained using Fourier analysis.

In conclusion, the optical fiber system is capable of filtering out high frequency noises very effectively. In addition to electrically isolating the SQUID systems from the power source, it can reduce the amount of electrical noise delivered to the system.

---

[Gol17] R. Golub, *The Systematics and Operational Studies (S.O.S) Apparatus justification document*, for DOE/NSF, 2017.

[Lam09] S. K. Lamoreaux and R. Golub, *J. Phys. G*, **36**, 104002 (2009).

# Research Based at CERN

Chapter 2



## 2.1 Tagging Quark and Gluon Jets Reconstructed by Particle Flow

P. AMORY, *Wellesley College, Wellesley, MA*; A.T. ARCE, I. RUFFIN, *Duke University, Durham, NC*

Quarks and gluons are some of the most common particles produced at the LHC. Both are seen in the detector as jets, with slight differences between the jets left by quarks (signal) and those left by gluons (background). Three taggers were created using TMVA to discriminate between quarks and gluons. These taggers used jets reconstructed by the particle flow algorithm as well as four substructure variables: 2-subjettiness, width, charged particle multiplicity, and the sum of transverse momenta ( $p_T$ ) of the charged particles in the jet. At an average of 50% signal efficiency, the particle-flow based taggers were able to produce a signal sample that is around 70-90% pure while rejecting around 80% of the background. It did slightly better than the canonical tagger using the EMTopo algorithm.

A jet is the signature left in a detector by a light quark or gluon. When these particles are produced, they undergo a quantum-chromodynamical process called fragmentation, where they decay into many particles, and eventually hadronization, where those particles combine into colorless hadrons. The hadrons are picked up by the detector. From there, jet reconstruction algorithms are responsible for deciding which particles are part of the jet and what the properties of the jet are (charge,  $p_T$ , etc.). There are various algorithms written for doing this. Most of them use information from only the tracking detector or the calorimeter. However, the particle flow algorithm uses information from both. It extrapolates the tracks into the calorimeter, associates the tracks with clusters, and then reconstructs the energy of the jet using calculations from the tracker. Particle flow is good for low- $p_T$  jets because the energy resolution of the tracker is very good at low  $p_T$ , and it is somewhat worse at high  $p_T$ . This project studied the algorithm's effectiveness in quark-gluon discrimination.

I used the Toolkit for Multivariate Data Analysis with ROOT (TMVA) to train three taggers: two neural networks and one boosted decision tree. Each of these taggers was trained using four variables, chosen for their discrimination between quark and gluon jets. Most of this discrimination relies on the fact that gluons carry more color charge than quarks. Because of this, they interact more strongly. Gluons undergo more fragmentation and hadronization than quarks, and they tend to form more spread-out jets containing more particles, while quarks tend to form more collimated jets with fewer particles inside [ATL12]. See Fig. 2.1 for the distributions of these variables.

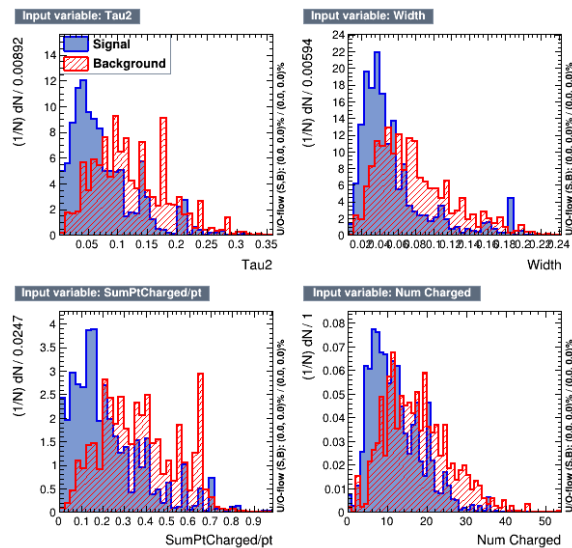


**Figure 2.1:** Depicted are the variable distributions used for the particle flow tagger. All four variables show clear separation that should be learned by the tagger.

The first variable used was the 2-subjettiness ( $\text{Tau}2$ ), or the probability that the jet in question is actually two jets clustered together. This tends to be higher for gluons, since gluon jets are more spread out and contain more particles than quark jets. Also, gluons are likely to decay to two quarks, which would form two jets.

The next variable used was the width:

$$\sum_{i=0} \frac{\Delta R_i p_{ti}}{p_{ti}}$$

where  $\Delta R$  is the angular distance between the jet axis and the  $i$ th component of the jet [ATL12]. The width is a measure of how spread out the energy is within the jet, and again, this should be higher for gluons than quarks.

The third variable is the number of charged objects. For the particle flow tagger, this is the number of charged particle flow objects, and for a comparison tagger based on EMTopo-reconstructed jets, this is the number of tracks. This number, the charged particle multiplicity, is one of the most powerful discriminants between quark and gluon jets.

The fourth variable is the sum of  $p_T$  of charged objects which measures how energetic the charged particles are within the jet. Again, it should be higher for gluons than quarks.

The tagger was tested on a Monte Carlo-generated sample of jets ranging from 50 GeV to about 2 TeV. A cut was placed at a value that would produce an average of 50% signal efficiency. The receiver operating characteristic (ROC) curve shown in Fig. 2.5 demonstrates that at 50% efficiency, the taggers should reject around 90% of the background.

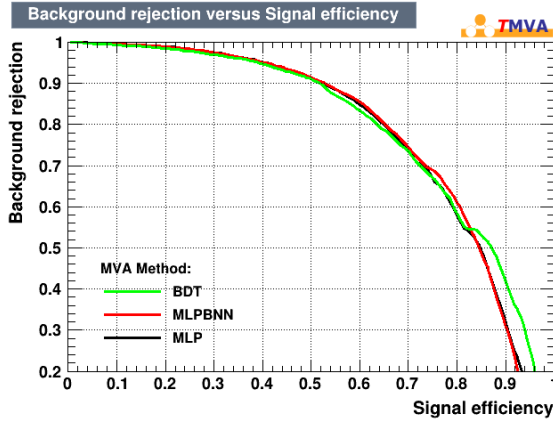


Figure 2.2: ROC curve showing the predicted performance of the particle-flow based tagger with the substructure variables mentioned above as inputs.

The tagger performance can be seen easily in Fig. 2.3. This shows purity, or the fraction of jets tagged as quarks that were actually quarks, as a function of  $p_T$ . It can be seen that the particle flow-based tagger does slightly better at all  $p_T$ , including low  $p_T$ , where it was predicted to do better. These differences are slight, but worth noticing. The taggers rejected around 80% of the background at 50% signal efficiency, again doing better for particle flow than for EMTopo (Fig. 2.4).

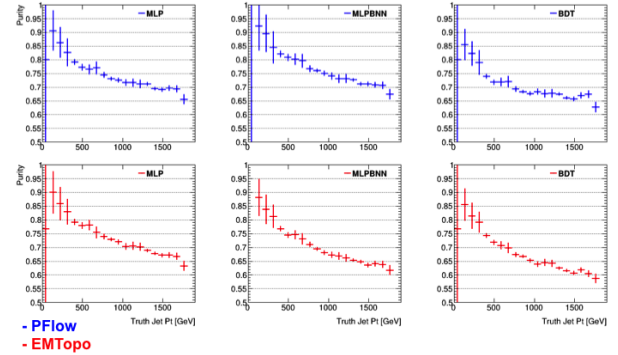


Figure 2.3: Signal purity as a function of  $p_T$  for particle flow (blue) and EMTopo (red) reconstructed jets. The particle flow tagger does better at all  $p_T$  and for all three methods, ranging from about 70% pure to about 90% pure.

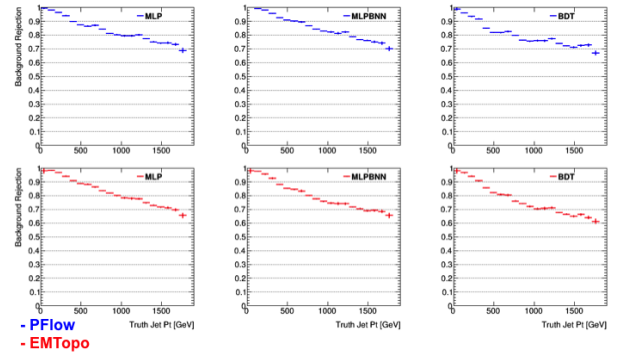


Figure 2.4: Background rejection as a function of  $p_T$  for particle flow (blue) and EMTopo (red) reconstructed jets. The particle flow taggers do better at all  $p_T$  and for all three methods, averaging about 80% background rejection.

The particle flow-based taggers were successful at purifying a sample of quarks and gluons to around 70-90%, depending on  $p_T$ . They did better than the EMTopo tagger created using similar substructure variables, albeit slightly. This tagger can hopefully be used in all kinds of applications, from new physics to Higgs studies - anything that involves quarks and gluons. In the future, this tagger could be optimized even more by including more or different variables or changing some of the machine learning parameters.

[ATL12] ATLAS Collaboration, Phys. Rev. D, **86**, 072006 (2012).

## 2.2 Identifying Quarks and Gluons Using Dijet Event Kinematics

A. BRODZELLER, *Bowling Green State University, Bowling Green, OH*; A. ARCE, I. RUFFIN, *Duke University*

Improving the classification of jets has many useful applications. Algorithms designed to tag jets can be utilized in searches beyond the standard model and for studies on jet substructure. A kinematic-based jet tagger can provide useful samples from real collision data that can be used in training and validating jet substructure-based taggers. A boosted decision tree classifier was trained using the Toolkit for Multivariate Analysis (TMVA) [Spe10] to identify quark-leading jets in dijet events by the event kinematics along with the subleading jet's mass. Evaluation of the kinematic jet classifier shows best performance at high  $\eta$  values and in the leading jet the  $P_T$  range of 1.5 TeV to 2.5 TeV.

Quarks and gluons produced in high energy proton-proton collisions rapidly fragment into groupings of collinear particles called jets. The jets can be identified through analysis of observables such as charged particle multiplicity, jet mass, and jet width. The jet can also be effectively treated as an object rather than a collection of particles and described using the kinematic observables. A classifying algorithm which tags jets as originating from a quark or a gluon using solely the kinematics can be applied to real collision data to obtain samples of primarily one type of jet. Purer samples would allow substructure-based taggers to be trained and evaluated on real data with intention of obtaining a higher tagging accuracy.

TMVA was used to train a machine learning method to identify events with quark-leading jets in a sample of simulated dijet events. The classifying methods were given the  $P_T$ ,  $\phi$  and  $\eta$  of both jets as well as the mass of the subleading jet. The dijet events were weighted such that TMVA trained the methods over an even distribution of leading jet  $P_T$  from 0 to 7 TeV. In order to identify the most robust and useful machine learning technique for development of a kinematic tagger, several of the neural networks and boosted decision tree (BDT) algorithms contained within TMVA were trained on the simulated data. As the input sample size increased, the BDT methods appeared most robust. The BDTF method, a boosted decision tree which utilizes a fisher discriminant to make cuts, slightly outperformed the other BDT methods. The goal was to reject 75% of the events with a gluon-leading jet while retaining above 30% of the events with a quark-leading jet. In Fig. 2.5, it can be seen that the BDTF was able to obtain the background rejection (leading gluon) of 75% when the signal (leading

quark) efficiency was about 40%.

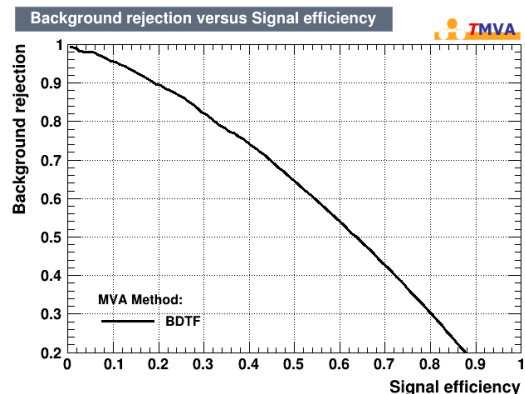


**Figure 2.5:** The Receiver Operating Characteristic (ROC) curve shows the performance of the BDTF classifier when implemented on a test sample of events. In this plot, signal is defined as events with a quark as the leading jet. Background is defined as events with a gluon leading jet.

After training the tagger with TMVA to the apparent maximum efficiency with the given variables, it was implemented on an evaluation set of previously unseen Monte Carlo simulated dijet events. These events were also weighted such that it was evaluating on an even distribution of leading jet  $P_T$ . When implemented over the entire range of  $P_T$  that the classifier was trained on, the tagger was able to reject 75% of events with a gluon leading jet while retaining 35% efficiency of correctly labeling events with a quark leading jet. Fig. 2.6 shows the accuracy of the tagger as a function of leading jet  $P_T$  and leading jet  $\eta$ . Over the entire set, the accuracy was about 60%, 10% greater than if the classifier was randomly guess-

ing while tagging. As seen in the figure, the BDTF was most accurate in the  $P_T$  range of 1.5 TeV to 2.5 TeV. It also obtained particularly high accuracy when tagging leading quark jets of high  $\eta$ .

Though the tagger was trained on events with a leading jet  $P_T$  as high as 7.5 TeV, it is important to note that with the current luminosity and collision energy of the Large Hadron Collider, the cross section for jets with a  $P_T$  higher than 3 TeV falls off rapidly and jets with  $P_T$  greater than 4 TeV are rarely observed. Thus, obtaining the greatest accuracy in the range noted above is heavily beneficial due to this being a range in which jets commonly occur. Another interesting feature of the tagger is its ability to tag with more accuracy at high  $\eta$  values. Quark jets tend to be more forward - they have high  $\eta$  values - so the higher accuracy of the tagger in these regions shows the BDTF was able to learn that feature about quark jets and apply it to the data it was given in the evaluation set.

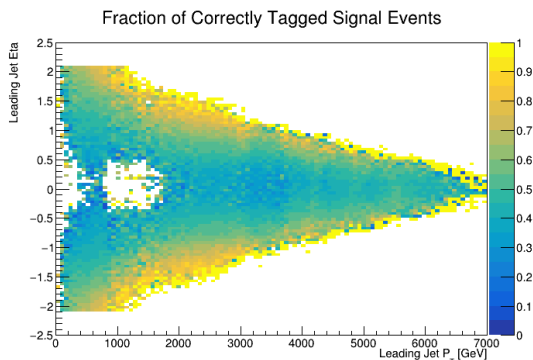


**Figure 2.6:** Evaluation of the BDTF tagger shows highest accuracy with leading jets of  $P_T$  between 1.5 and 2.5 TeV and leading jets with high values of  $\eta$ . Note that the hole in the graph is due to a gap in the data; It is not a feature of the BDTF algorithm

As mentioned earlier, the tagger was trained solely using the event kinematics and the subleading jet's mass. This allows the tagger to be a useful tool in verification of taggers which use substructure variables as discriminants. After applying the tagger to the evaluation set, the charged particle multiplicity was examined for both events tagged as leading quark and events tagged as leading gluon to look for the discrimination that should be present between the two types of jets. Gluons are theorized to fragment into a larger number of subsequent particles than quarks

due to the greater color charge. As a result, the average number of tracks, charged particle multiplicity, in a quark jet should be less than that in a gluon jet. This variable is often used a strong discriminant for taggers. Although the kinematic tagger did not use this variable while classifying, in Fig.2.7 there is a significant difference in number of tracks between events tagged as having a leading quark jet and those as having a leading gluon jet; Notably, gluon-tagged jets maintained a higher value of charged particle multiplicity than quark-tagged as expected.

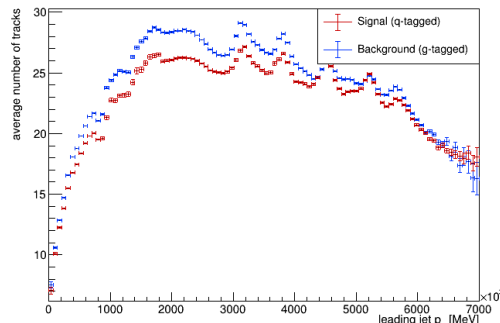


**Figure 2.7:** This figure shows the discrimination between events tagged as signal (leading quark) and events tagged as background (leading gluon) for charged particle multiplicity (number of tracks).

A kinematic-based leading jet tagger developed with a BDTF algorithm is able achieve an overall purity of 60% quark jets across leading jet  $P_T$  ranges of 0 to 7 TeV when given an evenly split dijet sample of leading quark jets and leading gluon jets. The tagger performs specifically well in middle range leading jet  $P_T$  and with dijet events which produce more forward-leading jets. The BDTF tagger was developed without including substructure observables of the leading jet but when applied to simulated data shows the expected discrimination between substructure observables such as charged particle multiplicity. Not having used substructure variables to tag, looking at these variables after tagging can provide useful information on the expected differences that should be seen in a gluon jet versus a quark jet. This information can then be used in training and validation for jet tagging algorithms which use substructure variables, such as charged particle multiplicity.

[Spe10] P. Speckmayer *et al.*, J. Phys. Conf. Ser., **219**, 032057 (2010).

## 2.3 Boosted Decision Trees Enhanced for Supersymmetry Search

A. GUTIERREZ, *University of Oregon, Eugene, OR*; M. EPLAND, A.T. ARCE, *Duke University*

One of the main goals of the LHC experiment is to search for evidence of supersymmetry (SUSY). Due to the large amount of data collected at the ATLAS detector, we need to find efficient techniques to improve the sensitivity of our search. In particular, we need ways to distinguish between a particular particle (signal) from the rest of our data (background). One technique that can be used to increase the efficiency of those searches is machine learning. Machine learning uses statistical analysis to give the computer the ability to “learn” from the data so that signal can be separated from background. In this project the possibility of detecting pairs of gluinos (which are the supersymmetric partners of gluons) through their hypothesized decays to multiple heavy top quarks was investigated by applying and comparing machine learning techniques such as TMVA, xgBoosted, and Sklearn in order to improve our efficiencies at the ATLAS detector.

The final detectable state that emerges from proton-proton collisions at the LHC consists of particles and jets which are reconstructed with high precision for physics analysis. The reconstructions come from direct energy deposition in our calorimeters and other indirect measurements. By applying conservation of angular momentum in the transverse plane of our detectors, we can indirectly detect particles that cannot be directly detected such as neutrinos. This particular type of measurement is key to the discovery of new physics. In this research project, the search for new physics is made by applying machine learning techniques to the gluino decay shown in Fig. 2.8. By comparing different machine learning techniques we can determine which one is more appropriate for gluino decay in hopes of finding evidence for SUSY.

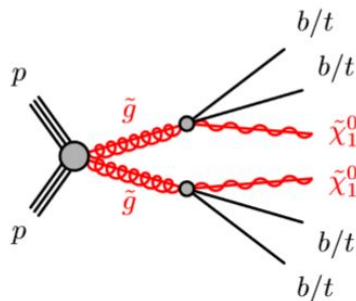


**Figure 2.8:** Hypothesized decay of gluino into Standard Model (SM) particles and two neutralinos.

For this project, three different machine learning techniques were used, namely, TMVA, xgBoosted, and Sklearn, all of which were tuned to deal with “Boosted Decision Trees” or BDTs. BDTs are employed in machine learning algorithms for regression and classification problems that produce a prediction model, relying on statistical analysis that uses Monte Carlo simulations to return “weights”. The weights give us positive (signal) and negative (background) values. In order to enhance the sensitivity, we can use machine learning techniques to teach the computer how to look for a particular event given some specific variables. The main signatures of the gluino decay are four or more “b-jets” and high transverse missing energy (MET). Fig. 2.9 shows an example of how weights are determined for different signatures. All three methods used same variables and similar parameters.

Once the BDTs have been trained, we get predicted scores that determine what signal and background are. After the training process is over, we use uncorrelated data to run a test of our algorithm and determine how accurate our results are with the true values obtained from our simulations. In particular, we can focus each technique to look over a specific mass range for both a gluino and a neutralino. Fig. 2.10 shows the accuracy obtained for individual pairs of gluinos and neutralinos. This procedure gives us the advantage of checking that our algorithm is indeed running over each possibility and gives us accuracy for events with high Lorentz-boosted top decays (boosted performance) and lower ones (compress performance).

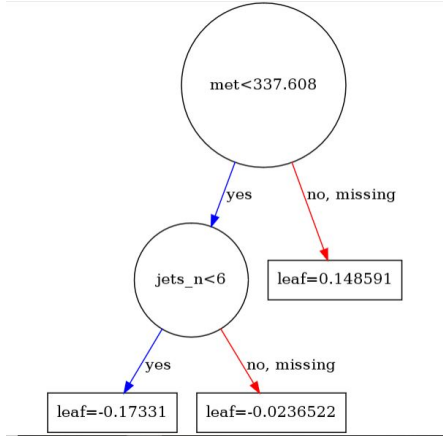


Figure 2.9: In this training process, positive values correspond to signal and negative correspond to background.

The minimum value of accuracy for xgBoosted, Sklearn, and TMVA was 88.59, 88.08, and 87.12% while their maximum value of accuracy was 98.85, 98.41, and 98.01% respectively. Depending on the type of search, we can determine what range of masses for the gluino and neutralino pair we are looking for. For each process we also find out their accuracy values for both high energetic (boosted) top decays and low (compress) decays. For compress decays all three methods performed within 0.01% of each other. On the contrary, for boosted decays xgBoosted was demonstrated to be more efficient than TMVA and Sklearn.

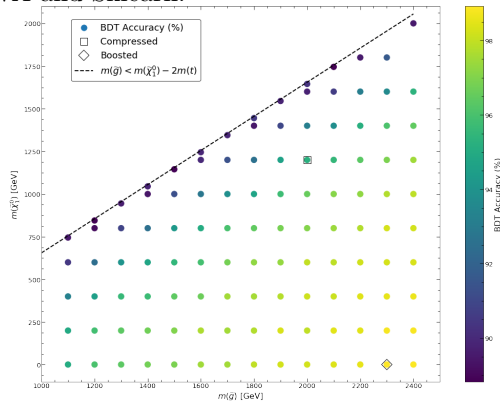


Figure 2.10: Plot of mass of gluino (x-axis) and neutralino (y-axis) versus accuracy using xgBoosted.

Fig. 2.11 shows the performance obtained for boosted decays; the x-axis shows how well we can detect our signal while the y-axis shows how well we reject background, zero being not signal or background at all and one being all our signal or background. Ideally we want to be on the lower right. As it can be

seen in Fig. 2.11, xgBoosted is 3.62% more efficient than Sklearn (while Sklearn is 0.002% more accurate than TMVA). A final study where all masses were taken into account (see Fig. 2.12) also demonstrated that in general, xgBoosted is the best choice for the signal study in this project.

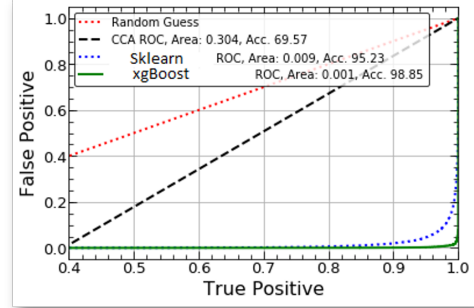


Figure 2.11: Performances of random guesses (red), simple variable restrictions (black), Sklearn (green), and xgBoosted (blue).

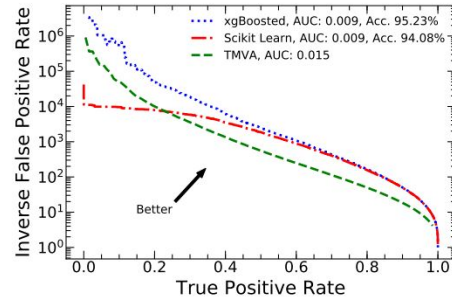


Figure 2.12: Plot of mass of gluino (x-axis) and neutralino (y-axis) versus accuracy using xgBoosted.

As it can be shown by the accuracies for all three methods, BDTs are very good at helping distinguish between our signal and background. Further studies on the parameters used in both TMVA and Sklearn may be able to improve their ability to discriminate between signal and background. Even for compress masses, xgBoosted, Sklearn, and TMVA perform similarly. This observation is important given that the lower the energy deposition in our detector the harder it is to separate signal versus background. A more complete study in which we compare all possible masses of gluinos and neutralinos shows that the performance of xgBoosted is better in comparison to both TMVA and Sklearn. Other studies have also shown that xgBoosted performs a faster training (although it requires more memory usage). Thus, xgBoosted is indeed more efficient for searches of gluino decay into SM particles and two neutralinos.

## 2.4 Study of backgrounds for $X \rightarrow W\gamma$ search at $\sqrt{S} = 13$ TeV

M. AZIZ, *Adelphi University, Garden City, NY*; A.T. GOSHAW, M. FENG, *Duke University*

The goal of the experiment was to study the backgrounds for known Standard Model processes by comparing the theory predictions with data obtained from the decay processes occurring at the Large Hadron Collider. The sensitivity of the search for new forces beyond those described by the Standard Model depend upon how well these backgrounds are understood. An invariant mass distribution of the outgoing partons of decay processes were generated from simulations describing the standard model predictions and compared to the invariant mass distribution of the data obtained from the LHC by taking the ratio. It was found the distribution generated from the simulation scaled by this ratio provided an accurate description of the standard model data background and could be used to extrapolate the data after a certain mass range.

All beyond standard model predictions introduce new bosons which result in new forces between standard model and beyond standard model particles [Eic08, AH01, Low17]. A generic search for these bosons can be done assuming some coupling to the standard model particles. The Large Hadron Collider at CERN is operating at 13 TeV proton-proton center-of-mass collision energy. There are searches being conducted by the ATLAS collaboration for a new heavy particle decaying to a W boson and a photon which would give evidence of a new force in addition to those described by the standard model [Aab18]. However the sensitivity of this search depends upon how well the background composed of known standard model processes is understood. Evidence of a new particle would be described by a resonance peak five standard deviations above the background invariant mass distribution at a certain mass range. Therefore, in order to be completely sure that the peak is not a statistical fluctuation, the background invariant mass distribution must be accurately described.

In order to compare the standard model theory predictions with data, Monte-Carlo simulations describing some standard model processes were generated by Minyu Feng. To generate these events a package called MadGraph was used. The Parton Distribution Function used was NNPDF23-lo-as-0130-qcd with the following kinematic cuts:  $\alpha_s(M_z) = 0.130$ , jet  $P_t = 100$  GeV, photon  $\eta < 2.5$  and jet  $\eta < 5$ . These events were also generated by splitting the photon transverse momentum into different slices and the values for number of events and cross section for each slice were determined using this package. All differ-

ent background processes were weighted the same.

The highest transverse momentum jet for either a quark or gluon was determined using equation 1:

$$P_t = \sqrt{p_x^2 + p_y^2} \quad (2.1)$$

Invariant mass calculations of the highest transverse momentum jet and photon were done on this Monte-Carlo sample using equation 2:

$$M = \sqrt{P_\mu P^\mu + Q_\mu Q^\mu + 2(P_\mu Q^\mu)} \quad (2.2)$$

The Monte-Carlo invariant mass distribution was fit using the following function:

$$f(x) = (1 - x)^{P_0} x^{P_1 + P_2 \log(x)} \quad (2.3)$$

The distribution was fit in three different ranges as shown in Fig. 2.13. The invariant mass distributions were generated for the data and the same fitting function was applied in different ranges. The incentive to fit the Monte Carlo in different ranges was to come up with a function to accurately describe the standard model processes. Thus the data used in the search for the X boson can be fit everywhere except the mass range where the search is being conducted. The fit around this range can be used to interpolate the background and a resonance peak can be compared with the background.

Another technique used to study the background was to compare the invariant mass distributions of the Monte Carlo and data by taking the ratio, as shown in Fig. 2.14. This ratio was fit to a third order polynomial of the form,  $f(x) = a + bx + cx^2 + dx^3$ . Each bin in the Monte-Carlo distribution was scaled with the value of this function at the center of the

bin. A superimposed plot of this new scaled distribution and the data are shown in Fig. 2.15. The ratio of the data with this scaled distribution is shown in Fig. 2.16.

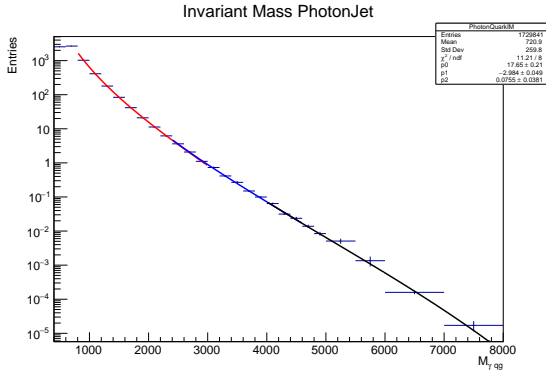


Figure 2.13: Sum of invariant mass fit in ranges 0.8-3 TeV with  $\chi^2 = \frac{11.21}{8}$ , 2.4-4.6 TeV with  $\chi^2 = \frac{15.87}{8}$  and 4-8 TeV with  $\chi^2 = \frac{12.67}{6}$ .

Fig. 2.13 shows some merit in the technique of modeling the background by fitting the data and Monte Carlo in different ranges. However Fig. 2.14 shows that the Monte Carlo by itself does not precisely model the data very well because the ratio of the data to the Monte Carlo is not unity in any range. Figs. 2.15 and 2.16 show that after the invariant mass distribution of the Monte Carlo was scaled by the third order polynomial fit, the new scaled distribution accurately describes the standard model background and can be used to extrapolate the data after a certain mass range.

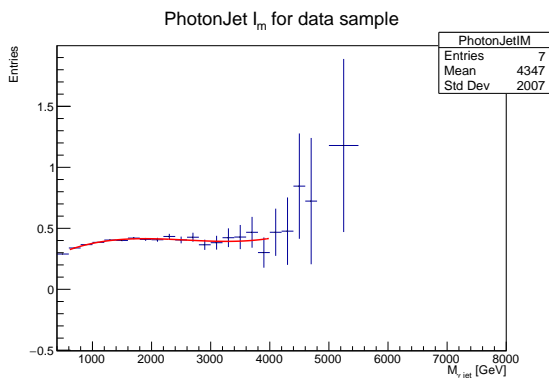


Figure 2.14: Ratio of data and Monte-Carlo distributions (blue) along with a third order polynomial fit (red).

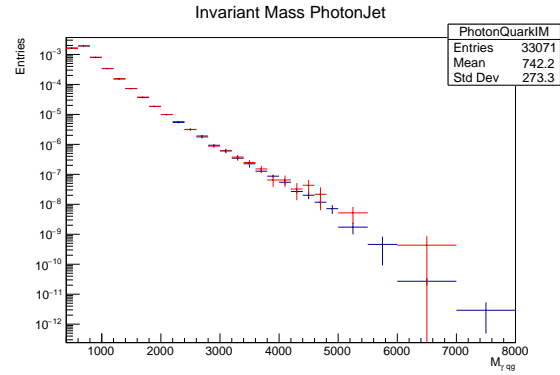


Figure 2.15: Data (red) superimposed with the scaled Monte-Carlo distribution (blue).

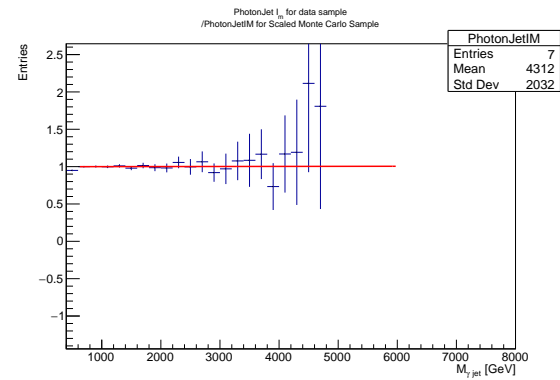


Figure 2.16: Ratio of data and scaled Monte Carlo.

Invariant mass distributions were made using a sliced Monte-Carlo sample and the data for the photon and the highest transverse momentum jet. These distributions were fit in different ranges in order to get a model for shape of the standard model background. The ratio of the invariant mass distribution of the data and the invariant mass distribution of the Monte Carlo was taken. This ratio was used to scale the Monte Carlo. It was found that this scaled Monte Carlo accurately described the standard model data background and can be used to extrapolate the data after a certain mass range. This work will be used by the ATLAS collaboration to model the background in the search for  $X \rightarrow W\gamma$  search at  $\sqrt{S} = 13$  TeV.

[Aab18] M. Aaboud *et al.*, (2018), arXiv:1805.01908.

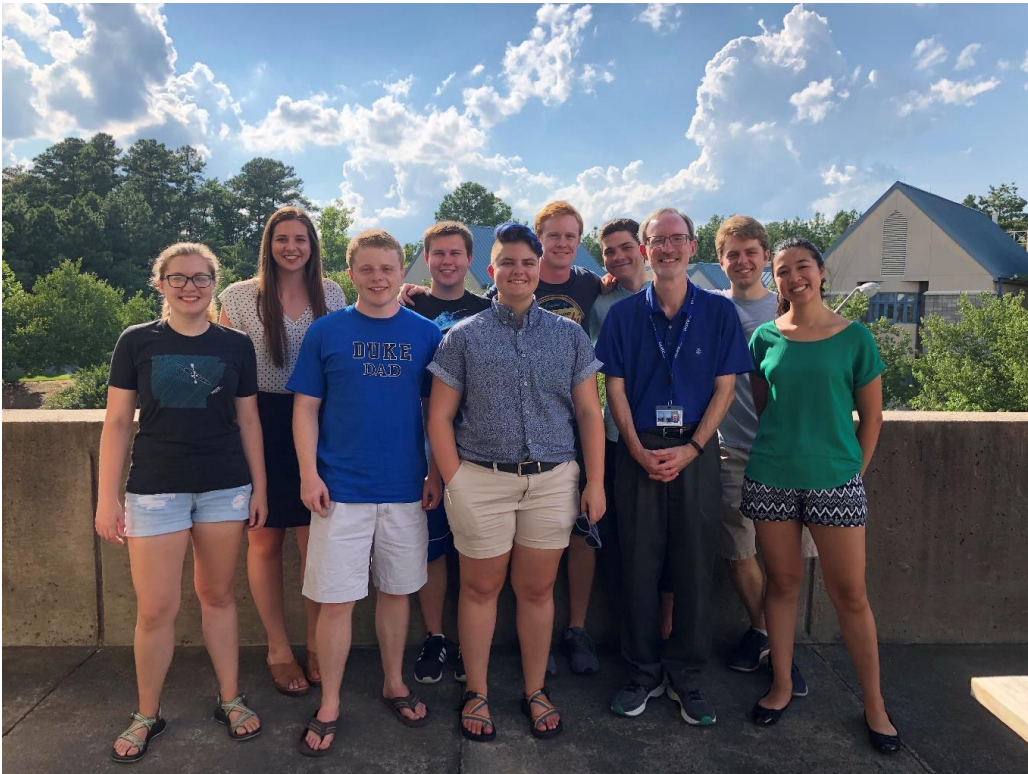
[AH01] N. Arkani-Hamed, A. G. Cohen, and H. Georgi, Phys. Lett., **B513**, 232 (2001).

[Eic08] E. Eichten and K. Lane, Phys. Lett., **B669**, 235 (2008).

[Low17] I. Low, J. Lykken, and G. Shaughnessy, Eur. Phys. J. C, **77**, 704 (2017).







# Index

Amory, P., 21  
Aziz, M., 27  
  
Brodzeller, A, 23  
  
Chappelow, T., 2  
  
Devaney, J.S., 10  
  
Giffin, P.W., 18  
Gutierrez, A., 25  
  
Hasan, H.C., 8  
  
Johnson, S.R., 6  
  
Koros, J., 12  
  
Parham, K., 14  
  
Wantz, A.J., 16  
Wegner, C., 4